THE JOURNAL OF PHYSICAL CHEMISTRY LETTERS
A JOURNAL OF THE AMERICAN CHEMICAL SOCIETY

pubs.acs.org/JPCL

Letter

Separating Orders of Response in Transient Absorption and Coherent Multidimensional Spectroscopy by Intensity Variation

Jacob J. Krich,*,# Luisa Brenneis,# Peter A. Rose, Katja Mayershofer, Simon Büttner, Julian Lüttig, Pavel Malý, and Tobias Brixner*

Cite This: J. Phys. Chem. Lett. 2025, 16, 5897−5905

Read Online

ACCESS | Metrics & More | Article Recommendations | Supporting Information

ABSTRACT: Interpretation of time-resolved spectroscopies such as transient absorption (TA) or two-dimensional (2D) spectroscopy often relies on the perturbative description of light−matter interaction. In many cases the third order of nonlinear response is the leading and desired term. When pulse amplitudes are high, higher orders of light−matter interaction can both distort lineshapes and dynamics and provide valuable information. Here, we present a general procedure to separately measure the nonlinear response orders in both TA and 2D spectroscopies, using linear combinations of intensity-dependent spectra. We analyze the residual contamination and random errors and show how to choose optimal intensities to minimize the total error in the extracted orders. For an experimental demonstration, we separate the nonlinear orders in the 2D electronic spectroscopy of squaraine polymers up to the 11th order.

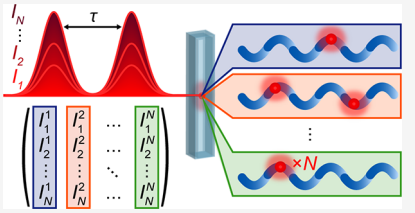

Nonlinear spectroscopies—from transient absorption (TA) to coherent multidimensional spectroscopies—require a careful balance when choosing the intensities of each pulse. In general, increasing pulse intensity improves the signal-to-noise ratio (SNR). The measured signal is commonly described as a power series in the amplitudes of the pulses[1] and spectroscopies are most commonly interpreted using the lowest-order term in that series. However, for larger pulse intensities the neglected higher-order terms provide a contamination of the desired signals, which physically represents extra interactions with the pulses. Such higher-order contamination distorts the signal spectral shape and dynamics and complicates the interpretation.

We recently showed that these orders of response can be separated in TA spectroscopy[2] and in excitation-frequency integrated 2D spectroscopy[3] using a procedure called "intensity cycling", enabling the extraction of third-order spectra even when using pulses intense enough to produce contaminated spectra. Furthermore, contributions from higher nonlinear orders can be separated and extracted, which reveal valuable information about multiply excited states and processes such as exciton−exciton annihilation.[2,4] In that intensity-cycling scheme, spectra are collected using N pump intensities I_p obeying the intensity cycling ratios, $I_p = 4I_0 \cos^2(\pi(p-1)/2N)$ for $p = 1, ..., N$, where I_0 is a base intensity. The first N response orders are extracted using formulas derived from the connection between TA spectra and n-quantum (nQ) signals that are frequently studied in two-dimensional electronic spectroscopy (2DES).[2,3,5,6] The nQ signals appear in the $-n\vec{k}_1 + n\vec{k}_2 + \vec{k}_3$ direction in a phase-matched 2DES experiment and are centered at $\omega_\tau = n\omega_0$ where ω_0 is the carrier frequency of the pump pulses (Figure 1), ω_τ is the excitation frequency, and $\vec{k}_i$ are the wavevectors of the optical pulses. Such nQ signals have been used to access higher-order responses,[5,7−11] beyond third order, as the leading order response increases with each multiple of ω_0. Intensity cycling also gives access to such higher-order signals using simpler TA measurements. Intensity cycling is in some aspects even superior to the nQ measurements since, as visualized in Figure 1, each nQ signal has contributions from many response orders, not only the leading $(2n + 1)^{\text{th}}$-order contribution; intensity cycling separates those contributions.

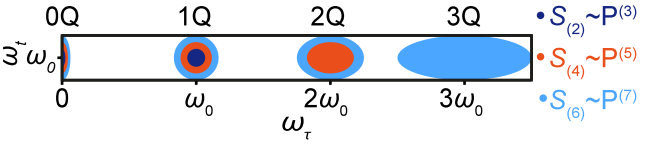

Figure 1. Schematic higher-order contributions in 2D spectra with a weak probe showing nQ signals at multiples of the carrier frequency ω_0, using excitation frequency ω_τ and detection frequency ω_t. The lowest-order contribution to each nQ signal is $S_{(2n)}$, which is $2n^{\text{th}}$ order in the pump amplitudes and order $2n + 1$ in the total field amplitude. The elongation along ω_τ of the nQ signal denotes the spectral width of the n^{th} harmonic of the excitation spectrum. For each nQ signal, there are several contributions of different orders. While only nQ signals with $\omega_\tau \geq 0$ are shown, equivalent nQ signals exist for $\omega_\tau < 0$.

Received: April 17, 2025
Revised: May 26, 2025
Accepted: May 30, 2025

https://doi.org/10.1021/acs.jpclett.5c01177
J. Phys. Chem. Lett. 2025, 16, 5897−5905

Here, we generalize from TA to coherently detected 2DES.[12−16] In this generalization, data collected with N pump intensities allows one to infer the first N response orders. We show three major conclusions from this generalization. First, the extraction of higher-order signals does not require the specific pump intensity ratios from the previously published intensity-cycling protocol but is feasible with arbitrary intensities. This generalization permits the reanalysis of previously collected and already published intensity-dependent data. Second, the nonlinear order separation is not limited to TA as in the prior scheme[2] but can also be applied to 2DES. Third, in the case where the pump pulses are identical except in arrival time, we quantify how random experimental noise and remaining contamination from unextracted higher orders affect the inferred response orders and use that theory to choose pump intensities that minimize the total error.

We demonstrate the technique experimentally on a squaraine copolymer $[SQA\text{-}SQB]_{18}$ (molecular structure shown in Supporting Information Figure S1), with an average of 18 dimer units,[9,17] and show the extraction up to the 11th order of response. Finally, we present self-consistency conditions to verify that the response orders have been correctly extracted.

We begin by defining the response orders and showing how they can be extracted. We consider a sequence of $L = 2$ (TA) or $L = 3$ (2DES) pulses which interact with the system. The electric field at time t and position $\vec{r}$ can be written in the vicinity of the sample as

$$\vec{E}(t, \vec{r}) = \sum_{l=1}^{L} \vec{e}_l \varepsilon_l \left(t - \frac{\vec{k}_l \cdot \vec{r}}{\omega_l} - t_l \right) e^{-i(\omega_l (t - t_l) - \vec{k}_l \cdot \vec{r})} + \text{c.c.} \tag{1}$$

where for pulse l, $\varepsilon_l(t)$ is the complex pulse envelope with any chirp included, ω_l is the central frequency, t_l is the arrival time, and $\vec{e}_l$ is the polarization, which can itself vary in space or time. We now focus on the case of coherently detected 2DES with $L = 3$ pulses and later show that the conclusions also apply to TA.

Consider that we vary the amplitude of the first two pulses, multiplying both ε_1 and ε_2 by a factor $\lambda > 0$ but leaving ε_3 unchanged. We do not need $\varepsilon_1(t)$ and $\varepsilon_2(t)$ to be identical. We further define a dimensionless intensity $I = \lambda^2$. We first write down the conclusion of how the signal scales with I and introduce a new notation $S_{(j)}$ to show the response orders in λ^j; we then motivate the form. In the absence of noise, the nonlinear signal can be written as

$$S(\tau, T, t, I) = \sum_{j=1}^{\infty} S_{(2j)}(\tau, T, t) I^j \tag{2}$$

where $\tau = t_2 - t_1$ is the coherence time, $T = t_3 - t_2$ is the population time, and t is the signal time, and we suppress the dependence of the signal on τ, T, and t for much of this discussion. For phase-matched TA and 2DES, $S_{(j)} = 0$ when j is odd. Consider that we want to extract the first N orders $S_{(2)}$ to $S_{(2N)}$ in eq 2. To this purpose, we define

$$S'(\tau, T, t, I) = \sum_{j=1}^{N} S_{(2j)}(\tau, T, t) I^j \tag{3}$$

where $S'(I) \approx S(I)$ if I is small enough that all terms $S_{(2j)} I^j$ are negligible for $j > N$. The orders $S_{(2j)}$ can be extracted by determining $S'(I)$ at N different intensities I_k with $k = 1, ..., N$, from which eq 3 implies

$$\begin{pmatrix} S'(I_1) \\ S'(I_2) \\ \vdots \\ S'(I_N) \end{pmatrix} = \begin{pmatrix} I_1 & I_1^2 & \dots & I_1^N \\ I_2 & I_2^2 & \dots & I_2^N \\ \vdots & & \ddots & \\ I_N & I_N^2 & & I_N^N \end{pmatrix} \begin{pmatrix} S_{(2)} \\ S_{(4)} \\ \vdots \\ S_{(2N)} \end{pmatrix} \tag{4}$$

We rewrite eq 4 as $S'(I_k) = \sum_n V_{kn} S_{(2n)}$, with $V_{kn} = I_k^n$. The matrix V is close to being a Vandermonde matrix, though it does not have the first column of ones in a conventional Vandermonde matrix because in coherently detected 2DES the pump-independent background is typically removed, resulting in $S_{(0)} = 0$. The inverse matrix V^{-1} allows extracting $S_{(2n)}$ from the $S'(I_k)$ as $S_{(2n)} = \sum_k V_{nk}^{-1} S'(I_k)$. But the measured data are $S(I_k)$ and not $S'(I_k)$, and the same procedure performed on the measured $S(I_k)$ gives inferred values of the $S_{(2n)}$, which we call $\hat{S}_{(2n)}$,

$$\hat{S}_{(2n)} \equiv \sum_{k=1}^{N} V_{nk}^{-1} S(I_k) \tag{5}$$

When noise and contamination beyond the truncation of eq 3 are negligible, the extracted $\hat{S}_{(2n)}$ equal the underlying $S_{(2n)}$. We show below how to estimate the contributions of both sources of error to $\hat{S}_{(2n)}$ for intensities I_k.

We now motivate eq 2 and describe the physical meaning of the expansion terms $S_{(n)}$ by connecting back to the standard theory of nonlinear spectroscopy. In a coherently detected measurement, the emitted electric field is determined by the induced nonlinear polarization $P^{(NL)}$ of the sample. For our derivation, we only need that the detected fields are proportional to $P^{(NL)}(\omega_t)$, but the proportionality can depend on ω_t, as long as it is independent of the pump-pulse parameters. For the present analysis, we use $P^{(NL)}$ as a proxy for the measured signal. The polarization $P^{(NL)} = P^{(3)} + P^{(5)} + ...$ can be written perturbatively in $E(t)$, see eq 1, in terms of system response functions $R^{(n)}$,[1] where for example

$$P^{(3)}(t) = \int dt_3 dt_2 dt_1 E(t - t_3) E(t - t_3 - t_2) E(t - t_3 - t_2 - t_1) R^{(3)}(t_3, t_2, t_1) \tag{6}$$

$$P^{(5)}(t) = \int dt_5 \dots dt_1 E(t - t_5) E(t - t_5 - t_4) E(...) E(...) E(...) R^{(5)}(t_5, \dots, t_1) \tag{7}$$

where we ignore the polarizations of the electric fields for simplicity. We now consider 2DES in a pump−probe geometry,[18] for which the phase-matching condition causes only odd orders to contribute to the signal. The order-separation technique is most straightforward in the weak-probe limit, where detected signals are proportional only to the first power of the probe amplitude ε_3; we consider that limit first and then generalize. When E in eqs 6 and 7 is expanded using eq 1, in every term that contributes to the signal, one of the E fields in eqs 6 or 7 must be a contribution from the probe $\varepsilon_3(t)$, and the other two or four E fields must be contributions from the pump pulses; combinations without ε_3 do not reach the detector, and combinations with higher powers of ε_3 are neglected in the weak-probe limit. In all terms that contribute to the signal, when ε_1 and ε_2 each scale with λ, it is easy to see

https://doi.org/10.1021/acs.jpclett.5c01177
J. Phys. Chem. Lett. 2025, 16, 5897−5905

that $P^{(2n+1)}$ scales with $\lambda^{2n} = I^n$. By comparison with eq 2, it follows that $S_{(2n)}I^n = P^{(2n+1)}$, so $S_{(2n)}$ reports on $R^{(2n+1)}$. Extracting the orders $S_{(2n)}$ using eq 4 is then equivalent to extracting the standard orders of response $R^{(2n+1)}$. In this notation, superscripts indicate orders of response in the total electric field and subscripts indicate orders of response in the electric field of the pulses whose amplitudes scale with λ—the pump pulses in our case.

If the probe pulse is strong enough that its contributions beyond first order are not negligible, then the mapping from $S_{(n)}$ to $R^{(m)}$ is less straightforward. In this case, $P^{(3)}$ is still linear in ε_3, but $P^{(5)}$ can have contributions that are linear or cubic in ε_3; quadratic contributions in ε_3 would not obey the phase-matching condition. We can break $P^{(5)}$ into portions that scale with $\lambda^2 = I$ and portions that scale with $\lambda^4 = I^2$. The former contributes to $S_{(2)}$ and is cubic in ε_3 while the latter contributes to $S_{(4)}$ and is linear in ε_1; example pathways contributing to both are shown in Figure 2. Pathways with n total pulse

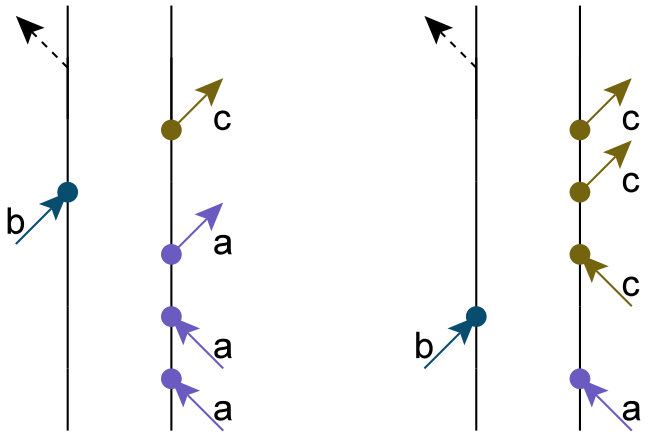

Figure 2. Two sample fifth-order pathways contributing to coherently detected 2D spectroscopy. While both pathways contribute to $R^{(5)}$, in an experiment in which the pump pulse (a,b) amplitudes are varied and the probe pulse (c) amplitude is unvaried, the left pathway contributes to $S_{(4)}$, and the right pathway contributes to $S_{(2)}$, as can be seen by counting the number of arrows containing either a or b. The right pathway only contributes significantly if the probe pulse is strong.

interactions contribute to $P^{(n)}$, and pathways that have $2n$ interactions with the pump pulses contribute to $S_{(2n)}$. In general, $P^{(2n+1)}$ contains terms that contribute to $S_{(2)}$, ..., $S_{(2n)}$. Conversely, $S_{(2n)}$ in principle has contributions from $P^{(2n+1)}$ and higher orders, though the probe must have high intensity for the higher orders to contribute significantly. TA spectroscopy ($L = 2$) with the pump intensity varied also obeys eq 2 (without a τ dependence) and the same connections between $S_{(n)}$ and $R^{(m)}$ as in 2DES.

In summary, $R^{(n)}$ is the usual n^{th}-order system response function with n being the order in the total applied electric field including pump and probe pulses. When the amplitudes of the pump pulses ε_1 and ε_2 are each scaled by the same factor λ, $S_{(n)}$ is the n^{th}-order response of the signal in λ. The particular pulse shapes defined in eq 1, i.e., without amplitude scaling ($\lambda = 1$), affect both $P^{(n)}$ (see eqs 6 and 7) and $S_{(n)}$. Similarly, note that extractions performed with eq 5 depend only on the ratios of the I_k; if all intensities I_k are expressed as multiples of a base intensity I_0, then $\hat{S}_{(2n)}$ extracted using eq 5 simply scales with I_0^n as I_0 varies, which we discuss further in Supporting Information Section S2.

Real optical pulses also have spatial profiles not described by eq 1, as in the usual case of focused pulses with Gaussian lateral profiles or even with spatial chirp. In the usual limit of local response,[1] where molecules each independently interact with the optical fields (e.g., see eq 5.13 in ref 1), the extraction that we describe here applies equally well to optical pulses with spatial profiles. As long as the entire pulse amplitude is scaled with the same factor λ, the extraction of response orders $S_{(2n)}$ is robust to spatial variation of the pulses as every molecule experiences the same ratios of pulse amplitudes, so they each individually obey eqs 6 and 7, and the scaling of these terms with λ^{2n} is the same for every molecule. The experimental works of refs 2 and 3 and this manuscript use probe pulses more tightly focused than the pump pulses, to ensure that the pump intensities are approximately uniform over the studied molecules; while this choice is helpful for interpretation, the extraction of the orders of response of the signals does not require it. Nonlocal effects, such as cascading processes,[19] are beyond the scope of the present work. We have previously found them not to be present in similar samples of equivalent optical depth.[2]

The intensity cycling method of ref 2 reduces to the form of eq 4, but eq 4 is more general because it shows that any sufficiently small intensities can work rather than only the specific intensity cycling ratios reported earlier. However, the new possibility of choosing arbitrary intensities raises the question of what intensities are optimal for extracting the $S_{(n)}$. Choosing intensities requires a balance between random and systematic errors. Higher pump intensity generally increases the signal and improves the SNR, but higher intensities also increase the systematic contamination error from higher-order terms in the truncated series of eq 2. We demonstrate how to find the optimal intensities that balance systematic and random error for TA and 2DES spectroscopies in the pump−probe geometry with identical pump pulses in the weak-probe limit. Consider that we are performing an N-intensity extraction of N orders up to $\hat{S}_{(2N)}$. Then we can write the measured signal $S(I)$ as

$$S(I) = S'(I) + c(N, I) + \eta \tag{8}$$

where $S'(I)$ is the ideal signal in the absence of contamination or random error in eq 3; $c(N, I) = \sum_{n=N+1}^{\infty} S_{(2n)} I^n$ is the systematic contamination error; and η is the random experimental error. Our goal is to choose the intensities to minimize $|\hat{S}_{(2n)} - S_{(2n)}|$ for some desired set of orders n.

We start by considering the random error with $c(N, I) = 0$ and consider the noise η_k on each experimental signal $S(I_k)$ to be independently chosen from a normal distribution with zero mean and standard deviation σ. This choice corresponds to the common case where noise is independent of pump intensity. We describe in Supporting Information Section S3 how we determine σ. We use standard error propagation techniques to determine the resulting root-mean-square random error $r_{(2n)} = \sqrt{(\hat{S}_{(2n)} - S_{(2n)})^2}$ in the estimate $\hat{S}_{(2n)}$. In that case, $r_{(2n)}$ is determined by the rows of V^{-1} as

$$r_{(2n)} = \sigma \sqrt{\sum_j (V_{nj}^{-1})^2} \tag{9}$$

When the intensities I_k are too close to each other, making V nearly degenerate, $r_{(2n)}$ can become large.

https://doi.org/10.1021/acs.jpclett.5c01177
J. Phys. Chem. Lett. 2025, 16, 5897−5905

We now consider the effects of higher-order contamination and demonstrate how to estimate $c(N, I)$ in 2DES from intensity-dependent TA measurements. Since TA data are faster to collect than 2DES, we use intensity-dependent TA spectra. These TA data allow us to estimate approximate values of both the separated orders for TA signals, $S^{\mathrm{TA}}_{(2n)}$, and for 2DES signals, $S^{\mathrm{2DES}}_{(2n)}$, including both the N orders we want to extract and some of the neglected higher orders. These estimates allow us to predict the optimal set of intensities that minimize the random and systematic error.

We use TA signals to estimate 2DES orders by exploiting a useful connection between the two signals. When $\tau = 0$, the 2DES experiment is identical to a TA experiment, since the two pump pulses each with intensity I coherently add, giving a single pump pulse with intensity $4I$. Therefore, $S^{\mathrm{2DES}}(\tau = 0, T, t, I) = S^{\mathrm{TA}}(T, t, 4I)$. The factor of 4 means that, upon Taylor expanding, $S^{\mathrm{2DES}}_{(2n)}(\tau = 0, T, \omega_t)I^n = 4^n S^{\mathrm{TA}}_{(2n)}(T, \omega_t)I^n$. We can also break the 2DES signal into its nQ pieces as

$$S^{\mathrm{2DES}}(\omega_\tau, T, \omega_t, I) = \sum_{n=-\infty}^{\infty} S^{n\mathrm{Q}}(\omega_\tau, T, \omega_t, I) \tag{10}$$

where the $S^{n\mathrm{Q}}$ for $n < 0$ are the Fourier conjugate partners of the $S^{n\mathrm{Q}}$ for $n > 0$ and do not contain extra information. The $\tau = 0$ 2DES signal can be obtained from a full integration over ω_τ from $-\infty$ to ∞, which means integrating across all of the nQ regions. When the nQ spectra are sufficiently spectrally separated from each other, integrating over a window at each nQ position in ω_τ in the 2D spectrum gives $S^{n\mathrm{Q}}(\tau = 0)$;[3] the $S^{n\mathrm{Q}}$ can also be separated at $\tau = 0$ using phase cycling.[2,20] Then, since $S_{(2n)}$ only contributes to rQ when $|r| \leq n$, we have $\sum_{r=-n}^{n} S^{r\mathrm{Q}}_{(2n)}(\tau = 0, T, \omega_t) = S^{\mathrm{2DES}}_{(2n)}(\tau = 0, T, \omega_t)$. We have shown previously that, for 2DES with identical pump pulses, $\varepsilon_1 = \varepsilon_2$,[2,3]

$$S^{r\mathrm{Q}}_{(2n)}(\tau = 0, T, \omega_t) = \binom{2n}{n-r} S^{n\mathrm{Q}}_{(2n)}(\tau = 0, T, \omega_t) \tag{11}$$

Noting that $\sum_{r=-n}^{n} \binom{2n}{n-r} = 4^n$ (see Supporting Information Section S4), we compare to eq 10 and conclude that

$$S^{\mathrm{TA}}_{(2n)}(T, \omega_t) = S^{n\mathrm{Q}}_{(2n)}(\tau = 0, T, \omega_t) \tag{12}$$

Equations 11 and 12 allow us to equate $S^{\mathrm{TA}}_{(2n)}(T, \omega_t)$ with the average value of $S^{r\mathrm{Q}}_{(2n)}(\omega_\tau, T, \omega_t)$ over its ω_τ spectral range. This connection means that if we know the contamination $c(N, I)$ in a TA measurement we can determine the average systematic contamination $c(N, I)$ for each nQ region in a 2D spectrum. We now show how to use a model for the intensity dependence of the TA signal to produce a model for the intensity dependence of the nQ signals at $\tau = 0$ via eqs 11 and 12, which we can then use to estimate $c(N, I)$ for ω_τ-integrated 2D measurements.

In many systems, TA signals saturate as pump intensity increases, with several possible saturation forms depending on the details of the studied system. For this discussion, we assume

$$S^{\mathrm{TA}}(T, \omega_t, I) = -S_{\max}(T, \omega_t)(1 - e^{-I/I_{\mathrm{sat}}(T, \omega_t)}) \tag{13}$$

where $S_{\max}(T, \omega_t)$ and $I_{\mathrm{sat}}(T, \omega_t)$ characterize the exponential saturation form.[21] We again suppress the T, ω_t dependence for the rest of this discussion. Using this saturation model, we derive an analytical model (see Supporting Information Section S5 for proof)

$$S^{n\mathrm{Q}}(\tau = 0, I) = \sum_{r=n}^{\infty} S^{n\mathrm{Q}}_{(2r)} I^r = S_{\max} \begin{cases} e^{-2I/I_{\mathrm{sat}}} \mathcal{I}_0(2I/I_{\mathrm{sat}}) - 1 & \text{for } n = 0 \\ (-1)^n e^{-2I/I_{\mathrm{sat}}} \mathcal{I}_n(2I/I_{\mathrm{sat}}) & \text{for } n \geq 1 \end{cases} \tag{14}$$

where $\mathcal{I}_n$ is the modified Bessel function of the first kind, with $S^{n\mathrm{Q}}(\tau = 0, I)$ plotted in Figure 3a. This form predicts that if the TA spectrum saturates like eq 13 then the $\tau = 0$ nQ spectrum for $n \geq 1$ has a maximum amplitude at finite I, unlike the TA signal itself. These maxima occur at 0.77, 2.28, 4.76, and 8.26 times I_{sat} for n = 1, 2, 3, and 4, respectively. Such maxima have not yet been observed, to our knowledge.

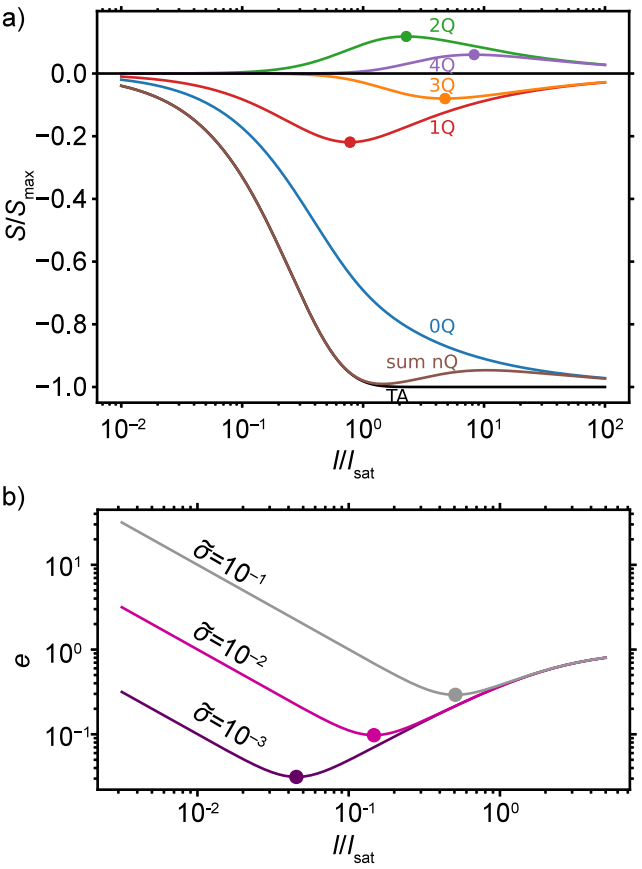

Figure 3. Choice of optimal intensities. (a) Saturation behavior of TA signals and nQ signals at $\tau = 0$. The TA and 0Q signals saturate at the same $S_{\max}$, while all nQ signals with $n \geq 1$ have maxima at finite intensity (circles). The TA signal is plotted as $S^{\mathrm{TA}}(4I)$ so the sum of the nQ signals for all n is the TA signal, as implied by eq 10. The sum of the nQ contributions from $n = -4$ to 4 is shown (brown), and it agrees well with the TA curve (black) up to I_{sat}. Including larger n would improve the agreement. (b) Error in extracting lowest-order TA signal as a function of pump intensity I for three values of saturated noise-to-signal ratio $\tilde{\sigma} = \sigma/S_{\max}$. At low intensities, random error dominates, while at higher intensities, the systematic error dominates. The minimum error (circles) occurs at lower I when $\tilde{\sigma}$ is smaller.

This exponential saturation form is frequently a good description of TA spectra, but the method described here can be applied to any model with a Taylor series that has a finite radius of convergence. For example, some systems obey a

https://doi.org/10.1021/acs.jpclett.5c01177
J. Phys. Chem. Lett. 2025, 16, 5897−5905

saturation model called "saturable absorption" in which $S^{\mathrm{TA}}(I) = -S_{\max}\frac{I}{I+I_{\mathrm{sat}}}$.[22,23] The Taylor series for saturable absorption only converges for $I < I_{\mathrm{sat}}$. In the Supporting Information Section S6.2, we show that order extraction can also work using a saturable absorption model.

The saturation form of eqs 13 and 14 allows us to determine the measured $\hat{S}_{(n)}$ that would be extracted from an experiment using N intensities I_k, where here we ignore the random error. Since we know the exact answers $S_{(n)}$ from the Taylor series of eq 14, we can determine the effect of contamination error on $\hat{S}_{(n)}$. For example, consider the nQ spectrum from eq 14. We evaluate $S^{n\mathrm{Q}}(\tau = 0, I_k)$ and use eq 5 to calculate the contaminated response orders $\hat{S}_{(2m)}$ for $m = 1, 2, \ldots, N$ from those N values. The systematic error in order $2n$ is $c_{(2n)} \equiv \hat{S}_{(2n)} - S_{(2n)}$.

We now combine the random and systematic errors by assuming that $r_{(2n)}$ and $c_{(2n)}$ are independent and add in quadrature. For either TA spectra or $\tau = 0$ nQ spectra, we define a total relative error e by taking the mean square error of $M \leq N$ orders

$$e^2 = \frac{1}{M}\sum_{n=1}^{M}\frac{r_{(2n)}^2 + c_{(2n)}^2}{S_{(2n)}^2} \tag{15}$$

For n where $S_{(2n)}$ is 0 we replace the denominator with 1, which gives the absolute error for that term; this condition occurs, for example, for $S^{2\mathrm{Q}}(I)$ where $S_{(2)}^{2Q} = 0$. Such absolute errors depend on the choice of I_0 that defines the intensity scale. With this definition for e, we then find the set of N intensities I_k that minimizes e. This procedure depends on $I_{\mathrm{sat}}(T, \omega_t)$ and $S_{\max}(T, \omega_t)$, so e can be minimized at a particular value of T and ω_t or averaged over them.

We first demonstrate this method to find the optimal intensity I for extracting the lowest-order TA signal $S_{(2)}^{\mathrm{TA}}$ with $N = 1$ intensity. In this case e has a simple form. The lowest-order term of the Taylor expansion of eq 13 is $S_{(2)}I = -S_{\max}I/I_{\mathrm{sat}}$. For a single choice of intensity there is no Vandermonde inversion, and $\hat{S}_{(2)} = -S_{\max}(1 - e^{-I/I_{\mathrm{sat}}})/I$. Then we find

$$e(\tilde{I}) = \sqrt{\left(\frac{\tilde{\sigma}}{\tilde{I}}\right)^2 + \left(\frac{\tilde{I} - 1 + \exp(-\tilde{I})}{\tilde{I}}\right)^2} \tag{16}$$

where $\tilde{\sigma} \equiv \sigma/S_{\max}$ and $\tilde{I} \equiv I/I_{\mathrm{sat}}$. Figure 3b shows eq 16, along with the optimal $\tilde{I}$, for three values of $\tilde{\sigma}$. The optimum (minimum) occurs at higher intensity when the noise is larger. We show the optimization of order extraction from TA spectra with multiple pump intensities in Supporting Information Section S6.3. We demonstrate the use of eq 15 for 2D spectra with the experimental results below.

As an experimental demonstration, we perform order separation in coherently detected 2DES of a squaraine copolymer, $[\mathrm{SQA\text{-}SQB}]_{18}$, in the weak-probe limit. The squaraine copolymer is dissolved in toluene, leading to the formation of a J-type polymer (see absorption spectrum in Figure 4a).[24] To choose our pulse intensities for 2DES, we begin with TA spectra with 101 different pulse intensities at a fixed pump−probe delay (i.e., population time) of $T = 2$ ps. We do not vary the pulse envelope shape or the spot size, so we refer to pulse intensities in this work by stating the energy per pulse. Pulse parameters and how they are determined are discussed in Supporting Information Section S7. We fit the dependence of the TA spectra on the pump intensity to the saturation form of eq 13, finding excellent agreement (Figure S2), with I_{sat} varying from 27 nJ to 106 nJ for $\hbar\omega_t$ from 1.50 to 1.76 eV. We optimize the error using I_{sat} at $\hbar\omega_t = A = 1.58$ eV corresponding to the maximum of the absorption spectrum, which yields $I_{\mathrm{sat}} = 46$ nJ and $S_{\max} = 0.054$. We use $\tilde{\sigma} = 9 \times 10^{-6}$ with $\sigma = 5 \times 10^{-7}$, as determined in Supporting Information Sections S3 and S6.1. Table 1 shows the minimal error e and optimal choices of intensities I_k for 1Q and 2Q spectra where

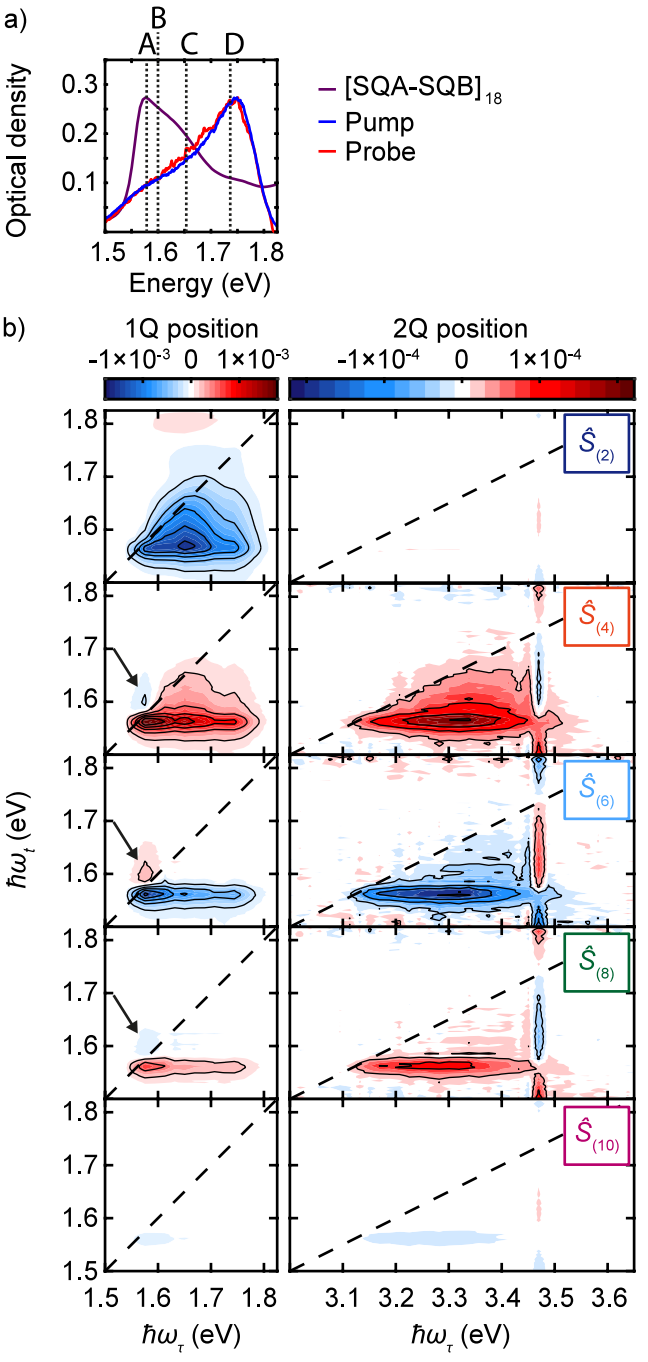

Figure 4. Extracted 2D spectra. (a) Absorption spectrum of $[\mathrm{SQA\text{-}SQB}]_{18}$ in toluene. The vertical dashed lines indicate spectral positions of features in the 2D spectra. (b) Extracted 1Q (left) and 2Q (right) 2D spectra of $[\mathrm{SQA\text{-}SQB}]_{18}$ in toluene up to $\hat{S}_{(10)}$ in the weak-probe limit. Diagonals (black dashed lines) are drawn at $\hbar\omega_\tau = \hbar\omega_t$ for the 1Q signal (left) and $\hbar\omega_\tau = 2\hbar\omega_t$ for the 2Q signal (right). Black arrows mark the NESA signals in the higher-order 1Q spectra, as defined in the text.

https://doi.org/10.1021/acs.jpclett.5c01177
J. Phys. Chem. Lett. 2025, 16, 5897−5905

Table 1. Errors in Extracting 1Q and 2Q Spectra at $\tau = 0$ Using Equation 15 for Several Choices of Number of Intensities N[a]

N		1Q error	Optimal I/I_{sat} for 1Q	2Q error	Optimal I/I_{sat} for 2Q
3		0.06	0.0149, 0.060, 0.095	0.14	0.018, 0.073, 0.12
4		0.037	0.023, 0.10, 0.18, 0.24	**0.064**	0.027, 0.12, 0.21, 0.27
5	I_{max} = 15 nJ	**0.029**	0.027, 0.12, 0.22, 0.30, 0.33	0.072	0.027, 0.12, 0.22, 0.30, 0.33
	$I_{max} = \infty$	0.021	0.030, 0.13, 0.26, 0.37, 0.44	0.040	0.033, 0.15, 0.29, 0.42, 0.49
6	I_{max} = 15 nJ	0.083	0.020, 0.088, 0.17, 0.25, 0.31, 0.33	0.21	0.020, 0.088, 0.17, 0.25, 0.31, 0.33
	$I_{max} = \infty$	0.014	0.035, 0.16, 0.33, 0.50, 0.63, 0.71	0.029	0.038, 0.18, 0.35, 0.54, 0.69, 0.77

[a]We use $\tilde{\sigma} = 9 \times 10^{-6}$, found in the spectra leading to Figure 4. We show optimal intensities for the case of unbounded I and also for the case where I is not allowed to exceed I_{max} = 15 nJ. For $N = 3$ or $N = 4$, the optimal I_k does not exceed the bound. Bold values show the minimal error achievable when I is bounded.

we are only interested in the accuracy of M = 3 orders, even when extracting $N >$ M orders. In general, increasing N improves the results. If, however, any of the optimal intensities exceeds the maximum pulse intensity experimentally available I_{max}, then we find an optimal N to minimize the error in the extraction, and further increases in N degrade the extractions. In our case, I_{max} = 15 nJ. Our value of I_{max} does not impact the error estimates for $N \leq 4$, but does change the error estimates for $N > 4$, with $N = 5$ being the optimal choice for 1Q signals. We use the $N = 5$ intensities from Table 1 that minimize the error in extracted 1Q orders, with intensities 1.2, 5.5, 10, 14, and 15 nJ. Note that while the optimal intensities are different for the 1Q and 2Q spectra, after optimal intensities exceed I_{max}, those differences become negligible, giving a clear set of intensities to use for both 1Q and 2Q spectral positions. Immediately after the intensity-dependent TA measurements to extract S_{max} and I_{sat} and random noise analysis, we carry out intensity-dependent 2D measurements while maintaining the same experimental conditions, such as pulse overlap, spot size, and laser spectra. The intensity-dependent 2DES at 1Q and 2Q positions are shown in Figure S4. We extract nonlinear orders from $\hat{S}_{(2)}$ to $\hat{S}_{(10)}$ using eq 5, with results at the 1Q and 2Q positions shown in Figure 4b, where the dimensionless intensities $\{I_k\}$ are obtained by dividing the pulse intensities by $I_0 = \frac{1}{N}\sum_{k=1}^{N} I_k = 9$ nJ (see Supporting Information Section S2). As required theoretically, the $\hat{S}_{(2)}$ contribution to the 2Q signal is small—essentially noise (upper right panel). We compare the extracted $\hat{S}_{(2)}$ to a low-intensity reference $\hat{S}_L$ in Figure S5, which shows differences only on the noise level.

The higher-order signals (Figure 4b) contain expected features as well as new information not present in low-order spectroscopies. With reference to the labels in Figure 4a, the dominant features in $\hat{S}^{1Q}_{(2)}$ are centered at $\hbar\omega_\tau = C = 1.65$ eV, slightly blueshifted compared to the main absorption peak at $A = 1.58$ eV, and the dominant features in $\hat{S}^{2Q}_{(4)}$ are at $\hbar\omega_\tau = 3.32$ eV, even more blueshifted compared to twice the energy of the absorption peak. These shifts could be due to the pump spectra, which are blue-weighted (Figure 4a). Unlike in the raw data (Figure S4), at each order the signs of the dominant features are identical in both 1Q and 2Q spectra (Figure 4), and those signs alternate with increasing order. This alternation was previously observed.[2] Reference 4 explained this sign change by showing that there are pathways contributing to $S_{2(n+1)}$ with the same (T, ω_t) evolution as for $S_{(2n)}$ but with opposite signs; it called these pathways "negations," such as a negated excited-state absorption (NESA) in $S_{(4)}$ that negates the standard ESA pathway in $S_{(2)}$. The 2DES were taken at $T = 2$ ps (Figure 4b), where the fifth-order 2Q signal reaches its maximum[2] and energy transfer within the singly excited manifold to the lowest-energy state has occurred.[25] The extracted 1Q spectra exhibit three prominent peaks on the excitation axis at $\hbar\omega_\tau = A$, C, and D. The spectral positions of the absolute signal maxima of $S^{1Q}_{(2n)}$ on the detection axis lie at $\hbar\omega_t = A$ and show no observable shift in ω_t with order. However, for $\hbar\omega_\tau >$ A, the signal with $\hbar\omega_t >$ A vanishes for increasing order, leading to a narrowed lineshape in ω_t direction. In contrast, the spectral position of the absolute signal maxima of the raw data (Figure S4) show an apparent blueshift in ω_t [from $\hbar\omega_t = 1.569$ eV (1.2 nJ) to 1.582 eV (15 nJ)] at high intensity, also observed in other systems.[26] This blueshift arises from the overlap of $\hat{S}_{(2n)}$ exhibiting different signs and lineshapes and not due to a ω_t shift in the $\hat{S}_{(2n)}$ themselves. The blueshift emphasizes the importance of higher-order separation, as even small contaminations can significantly affect the lineshape when the lowest-order signal is desired.

The high-order 1Q response reveals a pathway hidden in the leading-order 1Q spectrum. The higher-order 1Q signals exhibit a pronounced feature at $\hbar\omega_\tau = A$ and $\hbar\omega_t = B$ (black arrows, Figure 4b), which is not present in $\hat{S}^{1Q}_{(2)}$. In $\hat{S}^{1Q}_{n>2}$, these features exhibit an opposite sign compared to each order's most prominent feature, at (A, A), and they are not prominent in the raw data at any intensity (Figure S4). We previously demonstrated that a negative feature appearing in $\hat{S}_{(4)}$, which is not present in $\hat{S}_{(2)}$, can occur if 1-excitation signals are masked in $\hat{S}_{(2)}$ due to destructive interference of signal contributions.[4] Physically, one would expect an ESA peak at (A, B) in the $\hat{S}_{(2)}$ signal corresponding to pump excitation to the A exciton (Figure 4a) and probe excitation to a biexciton state at the frequency $A + B$. Supporting Information Section S10 uses a toy model to show that the NESA peak in $S^{1Q}_{(4)}$ is generally more visible than the ESA peak in $S^{1Q}_{(2)}$ when the A and B states arise from a weak coupling. While this manuscript is focused on the introduction of the high-order 2DES technique itself, this discussion shows just one piece of useful spectral information visible in the high-order and not in the leading-order spectra.

We now outline a procedure to verify that the response orders $\hat{S}_{(n)}$ have been correctly extracted with the chosen set of intensities $\{I_k\}$, independent of the model-based error analysis presented above. Equation 11 shows that the extracted orders $\hat{S}^{rQ}_{(2n)}(\tau = 0, T, \omega_t)/\binom{2n}{r}$ with fixed order n, should be equal at all T and ω_t, if $r \leq n$. Signals with $r > n$ should be zero. If these relations do not hold, it is model-independent evidence of error in $\hat{S}_{(2n)}$. We find $\hat{S}^{rQ}_{(2n)}(\tau = 0)$ by integrating $\hat{S}^{rQ}_{(2n)}(\omega_\tau)$, divide by $\binom{2n}{r}$ if $r \leq n$, and plot the results in Figure 5. Fulfilling the self-consistency check, the $\hat{S}^{rQ}_{(2)}$ for $r \geq 2$ are zero (Figure 5 top, green and orange curves), while the normalized 0Q and 1Q signals are equal (Figure 5 top, blue and red

https://doi.org/10.1021/acs.jpclett.5c01177
J. Phys. Chem. Lett. 2025, 16, 5897−5905

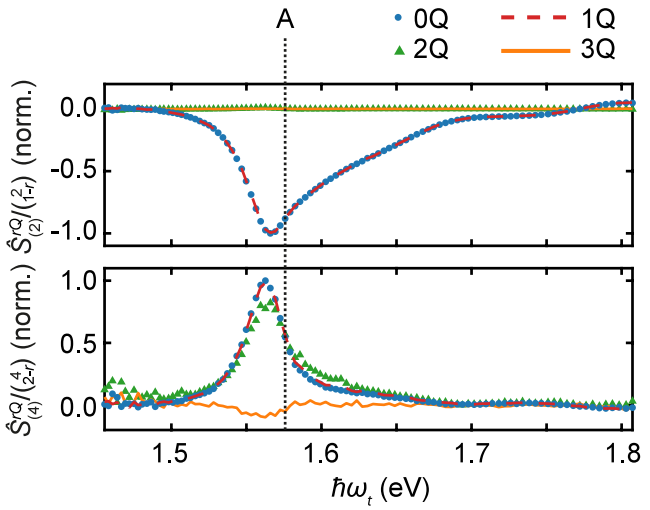

Figure 5. Self-consistency checks. $\hat{S}^{rQ}_{(2n)}/(_n{}^{2n}_{r})$ after window-integrating over ω_τ. When $r > n$, $\hat{S}^{rQ}_{(2n)}$ signals should be zero and are not scaled by $(_n{}^{2n}_{r})$. The integration windows are defined as $\omega_0[r - 1/2, r + 1/2]$ for $\omega_0 = 1.59$ eV. For each $n = 1, 2$, signals are normalized with respect to the absolute maximum values of $\hat{S}^{0Q}_{(2n)}$. The absorption maximum, marked by A as in Figure 4a, is the frequency at which S_{max} and I_{sat} were extracted when optimizing the pump intensities and is the frequency at which the errors in Table 1 were estimated.

curves). Similar to the lowest-order signal, the integrated and normalized extracted orders $\hat{S}^{0Q}_{(4)}$ and $\hat{S}^{1Q}_{(4)}$ overlap nearly perfectly (Figure 5 bottom, blue and red curves). The $\hat{S}^{2Q}_{(4)}$ signal shows some systematic deviation from the 0Q and 1Q (Figure 5 bottom, green curve), with a slight decrease of the peak at 1.56 eV and an increased blue shoulder indicating a small systematic error. One potential source of the remaining error comes from fluctuations of the applied pulse intensities. The $\hat{S}^{3Q}_{(4)}$ signal (Figure 5 bottom, orange curve) is supposed to be zero but shows a small deviation near 1.57 eV, indicative of contamination. Overall, the self-consistency checks demonstrate reasonable extraction of the nonlinear signals and support the conclusion that the lowest-order extractions $\hat{S}^{rQ}_{(2)}$ are essentially uncontaminated, while $\hat{S}^{rQ}_{(4)}$ have some contamination.

All signals in nonlinear spectroscopy strongly rely on the intensities of the excitation pulses. While a sufficiently high pulse intensity is necessary to measure a signal stronger than the noise level, higher-order terms that may be undesired can contribute to the measured signal. Here, we generalized the recently developed intensity-cycling method to not require specific intensity ratios between the spectra. As a result, the presented order-separation technique can be applied to previously collected intensity-dependent spectra. In addition, the new scheme is applicable not only to TA data, as in the previously reported extraction procedure, but can also be used to separate nonlinear orders in 2DES. We showed how to use the connection between TA spectra and excitation-frequency-integrated 2DES spectra to estimate the systematic errors in a high-order extraction and thus to choose optimal pump intensities for the extraction. We demonstrated the method on coherently detected 2DES measurements on squaraine copolymers $[SQA\text{-}SQB]_{18}$ in the weak-probe limit and showed that the high-order 1Q spectra reveal an ESA peak that is masked in the lowest-order spectrum. While we focus in this publication on TA and coherently detected 2D spectroscopy, the procedure presented here is readily adaptable to other spectroscopies such as transient grating, action-detected 2DES, or time-resolved photoemission spectroscopy.[27−31]

EXPERIMENTAL METHODS

The intensities and delays of the pump pulses were altered by an acousto-optic modulator pulse shaper on a shot-to-shot basis, which also chopped every second pump pulse, in a partially noncollinear pump−probe setup. The pump beam was blocked after the sample, and the probe beam was detected shot-to-shot via a spectrometer and line camera. For the correction of the 2D data, five 2D measurements with pump pulse energies (1.2, 5.5, 10, 14, 15) nJ were taken with the pulse shaper maintaining the same pulse envelope for each τ step. Simultaneously we measured a low-excitation-intensity reference at 0.16 nJ. All 2D spectra were taken with 299 steps in τ of step size 0.37 fs at a population time of $T = 2$ ps. For every average, all six 2D measurements were taken consecutively before repeating the pulse sequence. For setup details and signal processing see Supporting Information Sections S7 and S8.

ASSOCIATED CONTENT

Data Availability Statement

Data for all figures are available on Zenodo.[32]

Supporting Information

The Supporting Information is available free of charge at https://pubs.acs.org/doi/10.1021/acs.jpclett.5c01177.

Molecular structure, effects of choosing the base power, random error, connection between TA and 2DES signals, analytical saturation model for 2DES signals, choosing optimal intensities, experimental setup, raw data and data processing, comparison of lowest order with low-intensity reference measurement, and visibility enhancement of cross peaks in higher-order signals (PDF)

Transparent Peer Review report available (PDF)

AUTHOR INFORMATION

Corresponding Authors

Jacob J. Krich − *Department of Physics, University of Ottawa, Ottawa, ON K1N 6N5, Canada; Nexus for Quantum Technologies, University of Ottawa, Ottawa, ON K1N 6N5, Canada;* orcid.org/0000-0003-4514-0720; Email: jkrich@uottawa.ca

Tobias Brixner − *Institut für Physikalische und Theoretische Chemie, Universität Würzburg, Würzburg 97074, Germany; Center for Nanosystems Chemistry (CNC), Universität Würzburg, Würzburg 97074, Germany;* orcid.org/0000-0002-6529-704X; Email: tobias.brixner@uni-wuerzburg.de

Authors

Luisa Brenneis − *Institut für Physikalische und Theoretische Chemie, Universität Würzburg, Würzburg 97074, Germany*

Peter A. Rose − *Department of Physics, University of Ottawa, Ottawa, ON K1N 6N5, Canada;* orcid.org/0000-0003-0956-944X

Katja Mayershofer − *Institut für Physikalische und Theoretische Chemie, Universität Würzburg, Würzburg 97074, Germany*

https://doi.org/10.1021/acs.jpclett.5c01177
J. Phys. Chem. Lett. 2025, 16, 5897−5905

Simon Büttner − *Institut für Physikalische und Theoretische Chemie, Universität Würzburg, Würzburg 97074, Germany*
Julian Lüttig − *Department of Physics, University of Michigan, Ann Arbor, Michigan 48109, United States;* orcid.org/0009-0009-4926-2689
Pavel Malý − *Faculty of Mathematics and Physics, Charles University, 121 16 Prague, Czech Republic;* orcid.org/0000-0001-9244-9718

Complete contact information is available at: https://pubs.acs.org/10.1021/acs.jpclett.5c01177

Author Contributions

[#]J.J.K. and L.B. contributed equally to this work.

Notes

The authors declare no competing financial interest.

■ ACKNOWLEDGMENTS

We acknowledge funding by the European Research Council (ERC) within Advanced Grant IMPACTS (No. 101141366) and from the Natural Sciences and Engineering Research Council of Canada (NSERC) [597081-24]. P.M. acknowledges funding by Charles University (grant PRIMUS/24/SCI/007). We further thank Christoph Lambert and Arthur Turkin for providing the sample and its synthesis and Federico Gallina and Hugo Lafleur for careful reading of the manuscript.

■ REFERENCES

(1) Mukamel, S. *Principles of nonlinear optical spectroscopy*; Oxford, 1999.
(2) Malý, P.; Lüttig, J.; Rose, P. A.; Turkin, A.; Lambert, C.; Krich, J. J.; Brixner, T. Separating single- from multi-particle dynamics in nonlinear spectroscopy. *Nature* **2023**, *616*, 280−287.
(3) Lüttig, J.; Rose, P. A.; Malý, P.; Turkin, A.; Bühler, M.; Lambert, C.; Krich, J. J.; Brixner, T. High-order pump−probe and high-order two-dimensional electronic spectroscopy on the example of squaraine oligomers. *J. Chem. Phys.* **2023**, *158*, 234201.
(4) Rose, P. A.; Krich, J. J. Interpretations of high-order transient absorption spectroscopies. *J. Phys. Chem. Lett.* **2023**, *14*, 10849−10855.
(5) Heshmatpour, C.; Malevich, P.; Plasser, F.; Menger, M.; Lambert, C.; Šanda, F.; Hauer, J. Annihilation dynamics of molecular excitons measured at a single perturbative excitation energy. *J. Phys. Chem. Lett.* **2020**, *11*, 7776−7781.
(6) Lüttig, J.; Mueller, S.; Malý, P.; Krich, J. J.; Brixner, T. Higher-order multidimensional and pump−probe spectroscopies. *J. Phys. Chem. Lett.* **2023**, *14*, 7556−7573.
(7) Ding, F.; Fulmer, E. C.; Zanni, M. T. Heterodyned fifth-order two-dimensional IR spectroscopy: Third-quantum states and polarization selectivity. *J. Chem. Phys.* **2005**, *123*, 094502.
(8) Yu, S.; Titze, M.; Zhu, Y.; Liu, X.; Li, H. Observation of scalable and deterministic multi-atom Dicke states in an atomic vapor. *Opt. Lett.* **2019**, *44*, 2795.
(9) Malý, P.; Lüttig, J.; Turkin, A.; Dostál, J.; Lambert, C.; Brixner, T. From wavelike to sub-diffusive motion: exciton dynamics and interaction in squaraine copolymers of varying length. *Chem. Sci.* **2020**, *11*, 456−466.
(10) Brüggemann, B.; Pullerits, T. Nonperturbative modeling of fifth-order coherent multidimensional spectroscopy in light harvesting antennas. *New J. Phys.* **2011**, *13*, 025024.
(11) Turner, D. B.; Nelson, K. A. Coherent measurements of high-order electronic correlations in quantum wells. *Nature* **2010**, *466*, 1089−1092.
(12) Brixner, T.; Stenger, J.; Vaswani, H. M.; Cho, M.; Blankenship, R. E.; Fleming, G. R. Two-dimensional spectroscopy of electronic couplings in photosynthesis. *Nature* **2005**, *434*, 625−628.
(13) Oliver, T. A. A.; Lewis, N. H. C.; Fleming, G. R. Correlating the motion of electrons and nuclei with two-dimensional electronic−vibrational spectroscopy. *Proc. Natl. Acad. Sci. U.S.A.* **2014**, *111*, 10061−10066.
(14) Turner, D. B.; Wilk, K. E.; Curmi, P. M. G.; Scholes, G. D. Comparison of electronic and vibrational coherence measured by two-dimensional electronic spectroscopy. *J. Phys. Chem. Lett.* **2011**, *2*, 1904−1911.
(15) Fuller, F. D.; Ogilvie, J. P. Experimental implementations of two-dimensional Fourier transform electronic spectroscopy. *Annu. Rev. Phys. Chem.* **2015**, *66*, 667−690.
(16) Dostál, J.; Fennel, F.; Koch, F.; Herbst, S.; Würthner, F.; Brixner, T. Direct observation of exciton−exciton interactions. *Nat. Commun.* **2018**, *9*, 2466.
(17) Völker, S. F.; Dellermann, T.; Ceymann, H.; Holzapfel, M.; Lambert, C. Synthesis, electrochemical, and optical properties of low band gap homo- and copolymers based on squaraine dyes. *J. Polym. Sci., Part A: Polym. Chem.* **2014**, *52*, 890−911.
(18) Shim, S.-H.; Zanni, M. T. How to turn your pump-probe instrument into a multidimensional spectrometer: 2D IR and Vis spectroscopies via pulse shaping. *Phys. Chem. Chem. Phys.* **2009**, *11*, 748−761.
(19) Blank, D. A.; Kaufman, L. J.; Fleming, G. R. Fifth-order two-dimensional Raman spectra of CS_2 are dominated by third-order cascades. *J. Chem. Phys.* **1999**, *111*, 3105−3114.
(20) Tan, H.-S. Theory and phase-cycling scheme selection principles of collinear phase coherent multi-dimensional optical spectroscopy. *J. Chem. Phys.* **2008**, *129*, 124501.
(21) Diels, J.-C.; Rudolph, W. *Ultrashort laser pulse phenomena: fundamentals, techniques, and applications on a femtosecond time scale*, 2nd ed.; Academic Press Inc.: Amsterdam, 1996.
(22) Boyd, R. *Nonlinear Optics*; Academic Press, 2008.
(23) Kumar, N.; Cui, Q.; Ceballos, F.; He, D.; Wang, Y.; Zhao, H. Exciton-exciton annihilation in $MoSe_2$ monolayers. *Phys. Rev. B* **2014**, *89*, 125427.
(24) Völker, S. F.; Schmiedel, A.; Holzapfel, M.; Renziehausen, K.; Engel, V.; Lambert, C. Singlet-singlet exciton annihilation in an exciton-coupled squaraine-squaraine copolymer: a model toward hetero-J-aggregates. *J. Phys. Chem. C* **2014**, *118*, 17467−17482.
(25) Lambert, C.; Koch, F.; Völker, S. F.; Schmiedel, A.; Holzapfel, M.; Humeniuk, A.; Röhr, M. I. S.; Mitric, R.; Brixner, T. Energy transfer between squaraine polymer sections: From helix to zigzag and all the way back. *J. Am. Chem. Soc.* **2015**, *137*, 7851−7861.
(26) Novoderezhkin, V. I.; Razjivin, A. P. Multiexciton spectra of molecular aggregates: application to photosynthetic antenna complexes. *Phys. Chem. Chem. Phys.* **2024**, *26*, 23800−23810.
(27) Kahl, P.; Podbiel, D.; Schneider, C.; Makris, A.; Sindermann, S.; Witt, C.; Kilbane, D.; Hoegen, M. H.-v.; Aeschlimann, M.; zu Heringdorf, F. M. Direct observation of surface plasmon polariton propagation and interference by time-resolved imaging in normal-incidence two photon photoemission microscopy. *Plasmonics* **2018**, *13*, 239−246.
(28) Dąbrowski, M.; Dai, Y.; Petek, H. Ultrafast photoemission electron microscopy: Imaging plasmons in space and time. *Chem. Rev.* **2020**, *120*, 6247−6287.
(29) Huber, B.; Pres, S.; Wittmann, E.; Dietrich, L.; Luttig, J.; Fersch, D.; Krauss, E.; Friedrich, D.; Kern, J.; Lisinetskii, V.; Hensen, M.; Hecht, B.; Bratschitsch, R.; Riedle, E.; Brixner, T. Space- and time-resolved UV-to-NIR surface spectroscopy and 2D nanoscopy at 1 MHz repetition rate. *Rev. Sci. Instrum.* **2019**, *90*, 113103.
(30) Lv, B.; Qian, T.; Ding, H. Angle-resolved photoemission spectroscopy and its application to topological materials. *Nat. Rev. Phys.* **2019**, *1*, 609−626.
(31) Vogelsang, J.; Wittenbecher, L.; Mikaelsson, S.; Guo, C.; Sytcevich, I.; Viotti, A.-L.; Arnold, C. L.; L'Huillier, A.; Mikkelsen, A. Time-resolved photoemission electron microscopy on a ZnO surface using an extreme ultraviolet attosecond pulse pair. *Adv. Phys. Res.* **2024**, *3*, 2300122.

(32) Krich, J. J.; Brenneis, L.; Rose, P. A. Data for figures in "Separating orders of response in transient absorption and coherent multi-dimensional spectroscopy by intensity variation". *Zenodo* **2025**, DOI: 10.5281/zenodo.15519457.

https://doi.org/10.1021/acs.jpclett.5c01177
J. Phys. Chem. Lett. 2025, 16, 5897−5905

Supporting Information for Separating Orders of Response in Transient Absorption and Coherent Multidimensional Spectroscopy by Intensity Variation

Jacob J. Krich,[*,†,‡,#] Luisa Brenneis,[¶,#] Peter A. Rose,[†] Katja Mayershofer,[¶] Simon Büttner,[¶] Julian Lüttig,[§] Pavel Malý,[‖] and Tobias Brixner[*,¶,⊥]

†*Department of Physics, University of Ottawa, Ottawa, ON K1N 6N5, Canada*

‡*Nexus for Quantum Technologies, University of Ottawa, Ottawa, ON K1N 6N5, Canada*

¶*Institut für Physikalische und Theoretische Chemie, Universität Würzburg, 97074 Würzburg, Germany*

§*Department of Physics, University of Michigan, Ann Arbor, Michigan 48109, United States*

‖*Faculty of Mathematics and Physics, Charles University, 121 16 Prague, Czech Republic*

⊥*Center for Nanosystems Chemistry (CNC), Universität Würzburg, 97074 Würzburg, Germany*

#*Contributed equally to this work*

E-mail: jkrich@uottawa.ca; tobias.brixner@uni-wuerzburg.de

S1 Molecular structure

The experimental sample is a squaraine copolymer $[\text{SQA-SQB}]_{18}$ (Figure S1) dissolved in toluene. On average, the copolymer consists of 18 [SQA-SQB] dimer units; for details on the degree of polymerization, see Reference 1. The synthesis of the copolymer was carried out as described previously.[1,2]

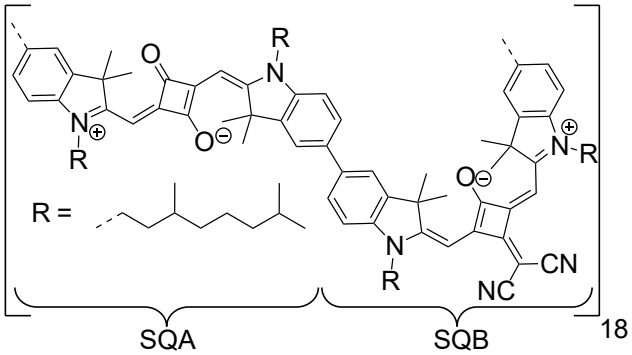

Figure S1: Chemical structure of the copolymer $[\text{SQA-SQB}]_{18}$, consisting on average of 18 [SQA-SQB] dimer units.

S2 Effects of choosing the base power

In the main text we discuss the order extraction using unitless intensities, as in Eq. 5. In such a case, the extracted orders $\hat{S}_{(n)}$ all have the same units. Nonetheless, the extracted orders depend on the choice of what intensity is labeled to be 1. Consider that we choose to scale intensities with the dimensionful intensity I_0. Then a pulse with dimensionful intensity $\bar{I}$ has dimensionless intensity $I = \bar{I}/I_0$. We here briefly discuss the impact of the choice of base intensity I_0. Reproducing Eq. 2 from the main text here,

$$S(\tau, T, t, I) = \sum_{j=1}^{\infty} S_{(2j)}(\tau, T, t) I^j, \tag{S1}$$

$$S(\tau, T, t, \bar{I}) = \sum_{j=1}^{\infty} S_{(2j)}(\tau, T, t) \left(\frac{\bar{I}}{I_0}\right)^j. \tag{S2}$$

We define

$$s_{(2j)} I_0^j = S_{(2j)}, \tag{S3}$$

which gives

$$S(\tau, T, t, I) = \sum_{j=1}^{\infty} s_{(2j)}(\tau, T, t) \bar{I}^j, \tag{S4}$$

which yields the expansion in terms of intensities with units. This form demonstrates that $S_{(2j)} \propto I_0^j$, and therefore the choice of I_0 scales the $S_{(2j)}$ by a factor of I_0^j, and so sets the scales for each extracted order. The choice of I_0 has no other effect on the measured quantities. In the main text and below, we refer to intensities I as having dimensions of nJ where we believe it is unambiguous; in such cases, the dimensionless intensities use $I_0 = 9$ nJ as a reference.

S3 Random error

For the random error η_k we determine the standard deviation in the raw 2DES data $S(I_k)$ by analyzing the low-intensity reference measurement. The data, collected for M different values of τ, is processed as described below in Section S8 to obtain the signal as a function of ω_τ. The goal is to find the contribution of random noise to $S^{n\mathrm{Q}}(\tau = 0)$, which are the objects for which Eq. 14 allows us to estimate the systematic error. We construct that noise by assuming that the noise at each of the M values of τ is independently chosen from a normal distribution with zero mean and standard deviation σ_τ. We cannot measure σ_τ easily in our data, but we can easily measure the noise σ_ω in ω_τ regions where no signal is expected. Here we show how the noise propagates into the frequency-domain signals and how measurement of the typical noise in a signal-free region of ω_τ can give the desired expected noise on $S^{n\mathrm{Q}}(\tau = 0)$. The result is Eq. S10, below.

In our signal analysis (Section S8), the data are reflected from positive to negative τ with the point at $\tau = 0$ not duplicated. We then have $M' = 2M - 1$ points along the τ axis. For this discussion, we use $S(\tau)$ to refer to the τ-domain signal and $\tilde{S}(\omega_\tau)$ to refer to the frequency-domain signal.

We choose to put the $1/M'$ normalization on the forward discrete Fourier transform,

$$\tilde{S}(\omega_\tau, T, \omega_t, I) = \frac{1}{M'} \sum_\tau S(\tau, T, \omega_t, I) e^{i\omega_\tau \tau}. \tag{S5}$$

The inverse discrete Fourier transform is then

$$S(\tau, T, \omega_t, I) = \sum_{\omega_\tau} \tilde{S}(\omega_\tau, T, \omega_t, I) e^{-i\omega_\tau \tau}. \tag{S6}$$

We choose this convention so that the $\tau = 0$ point is a simple sum of the frequency-domain signal,

$$S(\tau = 0, T, \omega_t, I) = \sum_{\omega_\tau} \tilde{S}(\omega_\tau, T, \omega_t, I). \tag{S7}$$

Similarly, if we wish to obtain the window-integrated nQ signals at $\tau = 0$, we take the restricted sum

$$S^{n\mathrm{Q}}(\tau = 0) = \sum_{\omega_\tau}{}' \tilde{S}(\omega_\tau), \tag{S8}$$

where the sum ranges depend on n.

After reflection, $S(\tau)$ is real and symmetric, which means that $\tilde{S}(\omega_\tau)$ is also real and symmetric. We can take the positive-frequency components as being independent normally distributed noise with standard deviation σ_ω. To find the variance σ_ω^2, we note that the variance of each η_k is σ_τ^2. Then from Eq. S5, the Fourier transform adds η_0 with variance σ_τ^2 to two times $\cos(\omega_\tau \tau_i)\eta_i$ for each of the $M - 1$ terms with $\tau_i > 0$. Each of those terms has variance $4\cos^2(\omega_\tau \tau_i)\sigma_\tau^2$. The variance of the sum can be found by replacing $\cos^2$ with $1/2$. Dividing by M' as in Eq. S5 gives

the root-mean-square (rms) noise amplitude at $\omega_\tau \neq 0$,

$$\sigma_\omega = \sigma_\tau \frac{\sqrt{1+2(M-1)}}{M'} = \frac{\sigma_\tau}{\sqrt{M'}} \tag{S9}$$

When summing over L positive frequencies, as in Eq. S8, the rms magnitude of the sum is $\sqrt{L}\sigma_\omega$, since the frequency-domain signals are approximately independent real quantities with standard deviation σ_ω. As a sanity check, we can sum over all frequencies to ensure that the noise in τ domain has standard deviation σ_τ. The noise at $\omega_\tau = 0$ has variance σ_ω^2. Each of the $M-1$ nonnegative frequencies is counted twice since the spectrum is symmetric and has variance $4\cos^2(\omega_\tau\tau)\sigma_\omega^2$. For $\tau \neq 0$, we can again approximate the $\cos^2$ as $1/2$, giving a total variance of $\sigma_\omega^2[1+2(M-1)] = \sigma_\omega^2 M'$, which is σ_τ^2, as desired, according to Eq. S9. There are in fact some subtle correlations in the frequency-domain noise to ensure that the variance at $\tau = 0$ is also σ_τ^2.

For the nQ signals at $\tau = 0$, we do not sum over all M' frequency points. If the nQ window has M'_{window} frequency points along ω_τ, the rms noise amplitude of $S^{n\text{Q}}(\tau = 0)$ is the sum of M'_{window} independent values of amplitude σ_ω, giving the σ we use in the main text of

$$\sigma = \sqrt{M'_{\text{window}}}\sigma_\omega. \tag{S10}$$

This result shows how to take an observed value of noise in frequency domain σ_ω and get the effective noise relevant to the signals in Eq. 14 of the main text.

Our goal is to estimate the noise in $S^{n\text{Q}}(\tau = 0)$, which is found by summing only over positive frequency bins. We determine σ_ω by computing the rms average signal in the region where $0.6\,\text{eV} < \omega_\tau < 0.9\,\text{eV}$ and $1.5\,\text{eV} < \omega_t < 1.8\,\text{eV}$, which is in between the 0Q and 1Q signals' spectral positions, and we consider it to be free of signal and to contain only noise. We find by eye that the signal fluctuates around zero and thus is dominated by noise. Any systematic signal present is expected to come from the wings of the 0Q and 1Q signals, and therefore to vary with ω_t. For each ω_t, we therefore compute the mean signal along the ω_τ-axis in this region. We subtract the mean, which is still a function of ω_t. We then compute the rms average of the signal over both ω_τ and ω_t in this region, assuming that the noise is independent of ω_t. We find $\sigma_\omega = 6.6 \times 10^{-8}$, so Eq. S10 gives $\sigma = 6 \times 10^{-7}$. We round this result to 5×10^{-7}. We have $M'_{\text{window}} = 85$, i.e., the number of pixels within the nQ regions ($\omega_0[n-1/2, n+1/2]$ for $\omega_0 = 1.59$ eV).

S4 Connection between TA and 2DES signals

We here discuss in more detail the derivation of Eq. 12, reproduced here:

$$S^{\text{TA}}_{(2n)}(T, \omega_t) = S^{n\text{Q}}_{(2n)}(\tau = 0, T, \omega_t). \tag{S11}$$

We begin with the identity $S^{\text{2DES}}(\tau = 0, I) = S^{\text{TA}}(4I)$, where the factor of four originates in the different conventions for labeling intensity in the same experiment. In 2DES, there are commonly two identical pump pulses, each of

intensity I. When they overlap at $\tau = 0$ they form a single pump pulse of intensity $4I$. In contrast, a TA experiment has only a single pump pulse, whose intensity is labeled I. Thus in order to compare results, the factor of 4 is needed. Expanding $S^{\mathrm{2DES}}(I) = \sum_n S^{\mathrm{2DES}}_{(2n)} I^n$ and $S^{\mathrm{TA}}(I) = \sum_n S^{\mathrm{TA}}_{(2n)} I^n$, it follows that $S^{\mathrm{2DES}}_{(2n)}(\tau = 0) = 4^n S^{\mathrm{TA}}_{(2n)}$. By the properties of the Fourier transform, we have that

$$S^{\mathrm{2DES}}_{(2n)}(\tau = 0) = \int d\omega_\tau S^{\mathrm{2DES}}_{(2n)}(\omega_\tau), \tag{S12}$$

which is equivalent to

$$S^{\mathrm{2DES}}_{(2n)}(\tau = 0) = \sum_{r=-\infty}^{\infty} S^{r\mathrm{Q}}_{(2n)}(\tau = 0), \tag{S13}$$

which includes $r < 0$ signals centered at $\omega_\tau < 0$. The integral and the sum are equivalent, so long as the windows used to integrate the rQ signals are contiguous and span the entire ω_τ axis. These nQ signals with $n < 0$ obey $\left[S^{-|n|Q}(-\omega_\tau)\right]^* = S^{|n|Q}(\omega_\tau)$, as required given that the time-domain signal in pump–probe geometry is real. The imaginary parts cancel upon full integration over ω_τ, or equivalently summing over all nQ. Then at each order we have

$$\sum_{r=-\infty}^{\infty} S^{r\mathrm{Q}}_{(2n)}(\tau = 0) = S^{n\mathrm{Q}}_{(2n)}(\tau = 0) \sum_{r=-n}^{n} \binom{2n}{n-|r|}, \tag{S14}$$

where the left-hand side comes from Eq. 11. We prove below that $\sum_{r=-n}^{n} \binom{2n}{n-|r|} = 4^n$, and we conclude that

$$\sum_{r=-\infty}^{\infty} S^{r\mathrm{Q}}_{(2n)}(\tau = 0) = 4^n S^{n\mathrm{Q}}_{(2n)}(\tau = 0) \tag{S15}$$

and so at each order we have

$$S^{n\mathrm{Q}}_{(2n)}(\tau = 0) = S^{\mathrm{TA}}_{(2n)}. \tag{S16}$$

We now prove that $\sum_{r=-n}^{n} \binom{2n}{n-|r|} = 4^n$ using the binomial theorem. We consider $(x+y)^{2n}$, which we expand as

$$(x+y)^{2n} = \sum_{k=0}^{2n} \binom{2n}{k} x^j y^{2n-j} = 2\sum_{k=0}^{n} \binom{2n}{k} x^j y^{2n-j} - \binom{2n}{n} \tag{S17}$$

where in the last equality we subtract the double-counted term when summing only to n instead of $2n$. Then let $x = y = 1$ and let $r = n - k$, so

$$4^n = 2\sum_{r=0}^{n} \binom{2n}{n-r} - \binom{2n}{n}. \tag{S18}$$

Note that for any function f_r, we have $2\sum_{r=0}^{n} f_r = f_0 + \sum_{r=-n}^{n} f_{|r|}$. We then have

$$4^n = \sum_{r=-n}^{n} \binom{2n}{n-|r|}. \tag{S19}$$

S5 Analytical saturation model for 2DES signals

Here we show that if the intensity-dependent TA signal follows an exponential saturation model as in Eq. 13, $S^{\mathrm{TA}}(T,\omega_t,I) = -S_{\max}(T,\omega_t)\left(1-e^{-I/I_{\mathrm{sat}}(T,\omega_t)}\right)$, then the nQ signals at $\tau = 0$ obey

$$S^{n\mathrm{Q}}(\tau=0,I) = \sum_{r=n}^{\infty} S^{n\mathrm{Q}}_{(2r)} I^r = S_{\max}\begin{cases} e^{-2I/I_{\mathrm{sat}}}\mathcal{I}_0(2I/I_{\mathrm{sat}}) - 1 & \text{for } n=0, \\ (-1)^r e^{-2I/I_{\mathrm{sat}}}\mathcal{I}_r(2I/I_{\mathrm{sat}}) & \text{for } n\geq 1, \end{cases} \tag{S20}$$

which is Eq. 14. We begin by taking the Taylor series of S^{TA} to get

$$S^{\mathrm{TA}}(I) = S_{\max}\sum_{j=1}^{\infty}\frac{(-1)^j}{j!}\left(\frac{I}{I_{\mathrm{sat}}}\right). \tag{S21}$$

From this form, we immediately have

$$S^{\mathrm{TA}}_{(2j)} = S_{\max}\frac{(-1)^j}{j!I^j_{\mathrm{sat}}}. \tag{S22}$$

Then using Eqs. 11 and 12 , we have $S^{r\mathrm{Q}}_{(2n)}(\tau=0) = \binom{2n}{n-r} S^{\mathrm{TA}}_{(2n)}$, which gives

$$S^{r\mathrm{Q}}_{(2n)}(\tau=0) = \binom{2n}{n-r} S_{\max}\frac{(-1)^n}{n!I^j_{\mathrm{sat}}} \tag{S23}$$

and therefore

$$S^{r\mathrm{Q}}(\tau=0,I) = S_{\max}\sum_{n=1}^{\infty}\binom{2n}{n-r}\frac{(-1)^n}{n!}\left(\frac{I}{I_{\mathrm{sat}}}\right)^n. \tag{S24}$$

This series can be summed in closed form, and Mathematica gives Eq. S20.

We note that this same procedure can be completed for any model $S^{\mathrm{TA}}(I)$, so long as it has a Taylor series with a finite radius of convergence, though a closed form may be impossible to find. For example, we demonstrate the same procedure for the case called "saturable absorption" in Section S6.2.

S6 Choosing optimal intensities

The main text presents the theoretical background for estimating random and systematic (contamination) errors for 2DES in the weak-probe limit, allowing determination of optimal intensities. Here, we show the details of the experimental procedure.

S6.1 Systematic error: exponential saturation

For the systematic error, we find the parameters I_{sat} and $S_{\max}$ from the saturation form of the TA spectra. We performed TA measurements for 101 linearly spaced excitation-pulse intensities between 0.27 nJ and 276 nJ at a population time $T = 2$ ps with identical pulse envelope shapes, with intensity controlled by the pulse shaper and all other experimental parameters kept unchanged. Figure S2a shows one such saturation curve, at the peak linear-

absorption energy $\hbar\omega_t = A = 1.58$ eV. A fit (grey line) to

$$S_{\mathrm{TA}}^{\mathrm{exponential}}(I) = -S_{\max}(1 - e^{-I/I_{\mathrm{sat}}}), \tag{S25}$$

which is Eq. 13, is shown. Figures S2b and c show $S_{\max}$ and I_{sat}, respectively, extracted from such a fit at each ω_t. We find I_{sat} ranging from 27 to 106 nJ and $S_{\max}$ ranging from 2.0 to 55.6 ΔmOD within the spectral range between 1.50 eV and 1.76 eV. Our goal is to choose $S_{\max}$ and I_{sat} that are typical for the spectrum and/or at an ω_t important for the 2D spectra. In the main text, we use the values at A, the peak in the absorption spectrum. The standard errors in the extracted parameters are smaller than 1.5 nJ and 0.2 ΔmOD for I_{sat} and $S_{\max}$, respectively, consistent with the high quality of the fits.

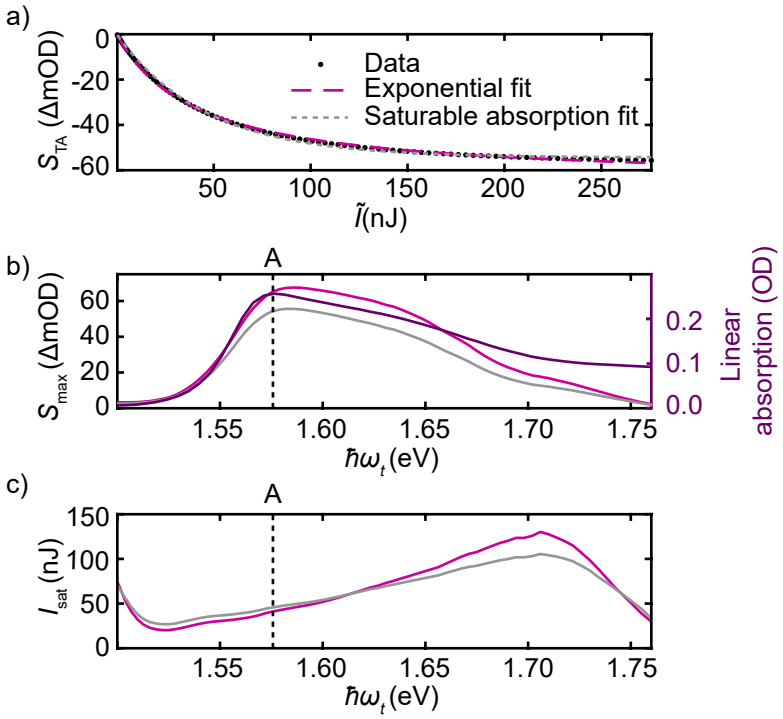

Figure S2: Systematic error estimation using power-dependent TA data. (a) Measured $S_{\mathrm{TA}}(I)$ at $\hbar\omega_t$=A= 1.58 eV and fit to Eq. 13 (grey) and Eq. S26 (magenta). (b) Fit parameter $S_{\max}$ for all ω_t and linear absorption spectrum. (c) Fit parameter I_{sat} for all ω_t. The dashed lines at 1.58 eV indicate the frequency shown in a, which is also used for the optimal intensity calculation.

S6.2 Systematic error: saturable absorption

While Figure S2a (grey line) shows the good quality of the exponential saturation form for fitting $S_{\mathrm{TA}}(I)$, we also consider saturable absorption, defined by

$$S_{\mathrm{TA}}^{\mathrm{sat}}(I) = -S_{\max}\frac{I}{I + I_{\mathrm{sat}}}. \tag{S26}$$

Just like $S_{\mathrm{TA}}^{\mathrm{exponential}}(I)$, this form has a known Taylor series, $S_{\mathrm{TA}}^{\mathrm{sat}}(I) = -S_{\max}\sum_{n=1}^{\infty}\left(\frac{-I}{I_{\mathrm{sat}}}\right)^n$. This power series is convergent only for $I < I_{\mathrm{sat}}$, unlike in Eq. S25. We now show how the analysis of the main text for exponential absorption can be straightforwardly adapted to $S_{\mathrm{TA}}^{\mathrm{sat}}$ to find the optimal intensities for a 2DES experiment focused on a particular nQ spectral region. Then we show how well our TA results fit Eq. S26 and the optimal intensities for 2DES suggested by those fits. Finally, we compare both saturation models with the extracted 2D data.

As in Eq. S23, we connect the TA response orders $S_{\mathrm{TA},(n)}^{\mathrm{sat}} = -S_{\max}(-1/I_{\mathrm{sat}})^n$ to the rQ response orders,

$$S_{(2n)}^{r\mathrm{Q}}(\tau=0) = \overbrace{-\frac{S_{\max}}{I_{\mathrm{sat}}^n}(-1)^n}^{S_{\mathrm{TA},(n)}^{\mathrm{sat}}}\binom{2n}{n-r}. \tag{S27}$$

Then letting $\tilde{I} \equiv I/I_{\mathrm{sat}}$,

$$S^{r\mathrm{Q}}(\tilde{I},\tau=0) = \sum_n S_{(2n)}^{r\mathrm{Q}}(\tau=0)I^n = S_{\max}\sum_n(-1)^{n+1}\binom{2n}{n-r}\tilde{I}^n = S_{\max}(-4\tilde{I})^r\left(\frac{1}{\left(\sqrt{4\tilde{I}+1}+1\right)^{2r}\sqrt{4\tilde{I}+1}} - \delta_{r0}\right), \tag{S28}$$

where δ_{ij} is the Kronecker delta function and the last identity comes from Mathematica. For saturable absorption, this new function replaces the modified Bessel functions that we found for exponential saturation. Note that $S^{r\mathrm{Q}}(\tilde{I},\tau=0)$ has a power series that is convergent only for $\tilde{I} < 1/4$.

For a given set of pump intensities $\{\tilde{I}_k\}$, we perform the Vandermonde extraction of $\hat{S}_{(2n)}^{r\mathrm{Q}}$ using Eq. 5 and define the systematic error as before, by comparing the Vandermonde-extracted $S_{(2n)}^{r\mathrm{Q}}(\tau=0)$ to the exact values in Eq. S27. We use the same noise σ as in Section S3. The updated optimal errors and pulse intensities are shown in Table S1, which is equivalent to Table 1 in the main text.

Table S1: Equivalent to Table 1 but using saturable absorption for the TA spectra instead of exponential saturation. Errors in $M = 3$ orders in 1Q and 2Q spectra at $\tau = 0$ for several choices of number of intensities N. We use $\tilde{\sigma} = 7.7 \times 10^{-6}$, with σ as in Section S3 and $S_{\max} = 0.065$ ΔOD.

N	1Q error	Optimal I/I_{sat} for 1Q	2Q error	Optimal I/I_{sat} for 2Q
3	0.15	0.0067, 0.027,0.043	0.22	0.0082, 0.033, 0.053
4	0.08	0.0092, 0.040, 0.074, 0.10	0.14	0.011, 0.047, 0.086, 0.11
5	0.06	0.011, 0.050, 0.097, 0.14, 0.17	0.11	0.012, 0.057, 0.11, 0.16, 0.19
6	0.05	0.012, 0.056, 0.11, 0.18, 0.23, 0.25	0.09	0.014, 0.063, 0.13, 0.20, 0.25, 0.28

For a system obeying saturable absorption, contamination errors are larger than for a system with exponential saturation, so the optimal intensities for order extraction are lower. Similarly, with fixed saturated noise-to-signal ratio $\tilde{\sigma}$, the minimum possible errors in order extraction are higher. These phenomena also mean the optimal intensity selection is less affected by $I_{\max}$. In our case, the optimal intensities do not exceed $I_{\max}$ until $N = 8$. We note that even though the power series for $S^{r\mathrm{Q}}(I,\tau=0)$ are divergent for $I > I_{\mathrm{sat}}/4$, the optimal intensities for order extraction can exceed $I_{\mathrm{sat}}/4$. Using the experimental intensities, which were chosen using the exponential saturation form, we find expected 1Q and 2Q errors of 0.29 and 0.39, respectively. This error is largely due to contamination, since the experimental intensities exceed I_{sat}.

Figure S2 shows that the intensity-dependent TA data are well fit by the exponential saturation form, Eq. 13, but the saturable form of Eq. S26 fits just as well. This observation raises the question whether the intensities used for the order extraction were, in fact, optimal. The 2D data must be consistent with the TA data when integrating over ω_τ. In particular, the two saturation forms make different predictions for $S^{rQ}_{(2n)}(\tau = 0)$,

$$S^{rQ}_{(2n),\mathrm{exp}}(\tau = 0) = \frac{S_{\max}}{I^n_{\mathrm{sat}}} \binom{2n}{n-r} \frac{(-1)^{n+1}}{n!}, \tag{S29}$$

$$S^{rQ}_{(2n),\mathrm{sat}}(\tau = 0) = \frac{S_{\max}}{I^n_{\mathrm{sat}}} \binom{2n}{n-r} (-1)^{n+1}. \tag{S30}$$

Equations S29 and S30 do not include the effects of systematic errors. Therefore, instead of comparing our extracted orders to these Taylor series expansions, we compare the experimental extracted orders to the theoretical extractions $\hat{S}^{rQ}_{(2n),\mathrm{exp}}$ and $\hat{S}^{rQ}_{(2n),\mathrm{sat}}$ that are obtained by evaluating the respective intensity-dependent models, equations S20 and S28, at the experimental pulse intensities, and applying Eq. 5 of the main text. Using the extracted $S^{rQ}_{(2n)}(\omega_\tau, T, \omega_t)$, we window-integrate over ω_τ to obtain $S^{rQ}_n(\tau = 0, T, \omega_t)$. We compare the experimental results to $\hat{S}^{rQ}_{(2n),\mathrm{exp}}$ and $\hat{S}^{rQ}_{(2n),\mathrm{sat}}$ with fixed r and varying n. Figure S3 shows the $\hat{S}^{rQ}_{(2n)}(\tau = 0, T, \omega_t)$ at $T = 2$ ps and $I_0 = 9$ nJ for $\omega_t = 1.57$ eV and 1.58 eV along with $\hat{S}^{rQ}_{(2n),\mathrm{exp}}(\tau = 0)$ and $\hat{S}^{rQ}_{(2n),\mathrm{sat}}(\tau = 0)$, where I_{sat} is determined by the fits shown in Figure S2. Note that $S^{2Q}_{(2)} = 0$, so the model signals there are entirely due to contamination error.

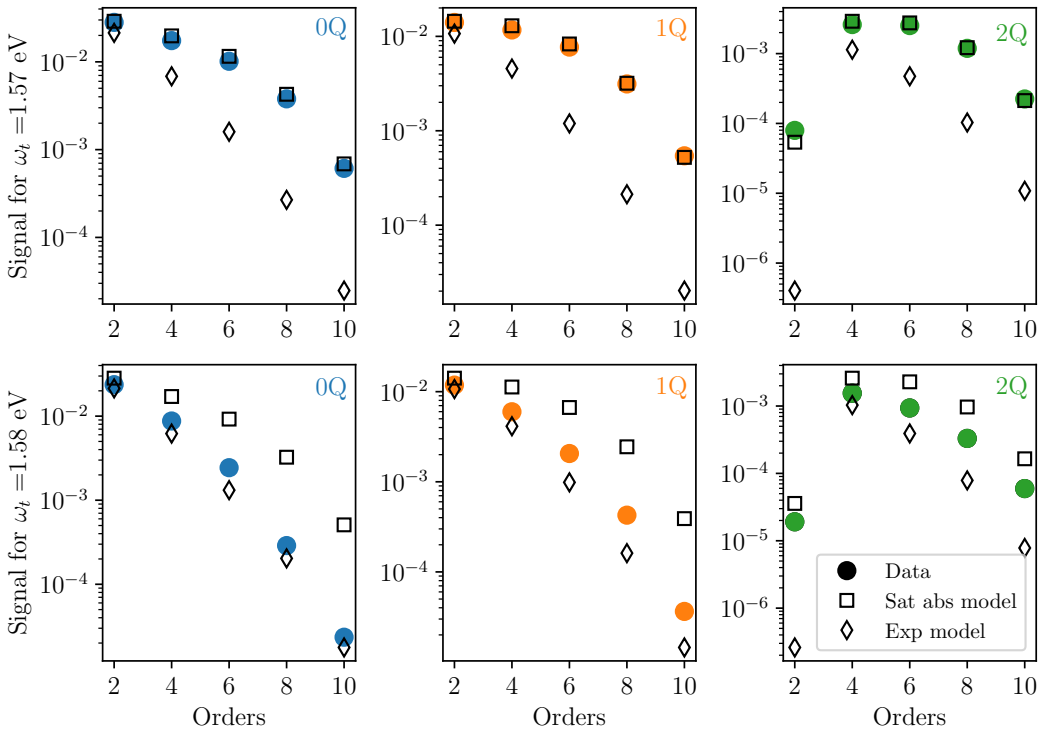

Figure S3: Comparison of saturation models. Integrated spectral regions of the 0Q-2Q signals ($\omega_0[r - 1/2, r + 1/2]$ for $\omega_0 = 1.59$ eV) at $T = 2$ ps and $I_0 = 9$ nJ and predictions from two saturation models: Exponential saturation model ($\hat{S}^{rQ}_{(2n),\mathrm{exp}}(\tau = 0)$, diamonds) described by Eq. S29 and saturable absorption model ($\hat{S}^{rQ}_{(2n),\mathrm{sat}}(\tau = 0)$, squares), described by Eq. S30.

Figure S3 shows that the experimental data agree better with the saturable absorption model at $\omega_t = 1.57$ eV, while the data seem to agree better with the exponential saturation model at $\omega_t = 1.58$ eV. In some spectral regions neither model fits well. We do not believe that either saturation form is precisely accurate but rather that they serve as guides to aid in the selection of optimal intensities. We do not anticipate perfect agreement of extracted orders with the predictions of either model. We conclude that either model can be used for this set of data.

S6.3 Optimization for TA spectroscopy

We consider now the optimization of intensities for extraction of $M = 3$ orders in TA spectroscopy, rather than for nQ 2DES. The process of estimating the contamination error is the same as described in the main text, but we use the saturation form for TA spectra (e.g., Eq. 13 or Eq. S26) in place of the saturation form for nQ spectra (Eq. 14 or Eq. S28). We illustrate here for the exponential saturation case, Eq. 13. For the random noise distribution, we use $\sigma_\tau = \sqrt{M'}\sigma_\omega = 1.6 \times 10^{-6}$ with σ_ω as determined in Section S3, which gives $\tilde{\sigma} = 3.0 \times 10^{-5}$. Then the optimal errors and intensities for the TA measurement are shown in Table S2. These TA pump intensities are similar to those obtained at $\tau = 0$ from the 1Q 2D pump intensities in Table 1, which produce a TA pulse with four times larger intensity.

Table S2: Equivalent to Table 1 but for extraction of orders of the TA signal rather than of nQ signals, using the exponential saturation form of the TA spectra. Errors in $M = 3$ orders for several choices of number of intensities N.

N	TA error	Optimal I/I_{sat}
3	0.094	0.055, 0.22, 0.35
4	0.036	0.085, 0.37, 0.67, 0.86
5	0.020	0.11, 0.49, 0.96, 1.4, 1.6
6	0.013	0.13, 0.60, 1.2, 1.8, 2.3, 2.6

S7 Experimental setup

The TA measurements are taken with a partially noncollinear pump–probe setup. The output of a commercial Yb-laser (PHAROS, Light Conversion) is spectrally broadened with a commercial non-collinear optical parametric amplifier (ORPHEUS, Light Conversion) and yields pulses with a spectral range from 550 nm to 840 nm at a repetition rate of 50 kHz. The amplified output is then split (178892, Layertec GMbH), with 90% of the intensity in the pump beam and the remaining 10% in the probe beam. The probe pulse is compressed by two fused silica prisms and time delayed by a mechanical stage (M-IMS1000LM-S, Newport) to adjust the population time T. The pump pulse is pre-compressed by two BK7 prisms and then compressed by an acousto-optic modulator (AOM) pulse shaper (Quickshape, PhaseTech) that also generates coherent double pulses with variable inter-pulse delays for the 2D measurements. The pump pulse has a duration of $\tau_p = 14$ fs (intensity FWHM) after compression, characterized via a collinear frequency resolved optical gating (FROG) setup. The spectral region from 550 nm to 660 nm is blocked in the prism compressor setups for both beams. After compression, both beams are focused in the sample position and have beam radii of $r_x = 43$ µm and $r_y = 38$ µm for the probe and $r_x = 67$ µm and $r_y = 172$ µm for the pump

beam at a limit of e^{-1} of the maximum amplitude. The pump beam is blocked after passing through the sample, and the probe beam is detected on a shot-to-shot basis with a spectrometer (Spektrometer Acton 2156, Princeton Instruments) and line camera (HS-Kamera Serie3030, Entwicklungsbüro Stresing). The data are taken and evaluated with custom LabView 2021 and Matlab R2023b scripts. For the extraction of response orders of the 2D data, a total of six 2D measurements at different pump powers were taken. Each 2D spectrum was recorded while scanning the time delay τ between two pump pulses over $M = 299$ steps with a step size of 0.37 fs. The population time was set to $T = 2$ ps. First the full 2D spectrum was measured before the intensity was changed. The pump-pulse energies E_p were set to 15 nJ, 14 nJ, 10 nJ, 5.5 nJ, 1.2 nJ, and 0.16 nJ, chosen according to the optimal intensity procedure described in the main text and in Section S6. The pump-pulse energies were determined by measuring the pulse energy of both excitation pulses at $\tau = 0$ fs and dividing them by four to obtain the intensity of a single pump pulse. The first five 2D spectra were used for the extraction of the different orders, while the measurement at the lowest pump energy is used as low-intensity reference. In this work we refer to the intensities by stating the pulse energies as we do not vary the pump pulse envelope shape or the spot size. The maximum pulse intensities are given within the approximation of a Gaussian beam by

$$I_{\text{pump}} = \frac{4E_p}{\tau_p r_x r_y}\sqrt{\frac{\ln 2}{\pi^3}}, \tag{S31}$$

which yields the peak pulse intensities listed in Table S3.

Table S3: Pulse energies and pulse intensities of a single pump pulse in 2D experiments.

E_p (nJ)	I_{pump} (GWcm^{-2})
15	5.6
14	5.1
10	3.7
5.5	2.0
1.2	0.46
0.16	0.058

S8 Raw data and data processing

Before extracting the higher-order spectra discussed in the main manuscript, we apply the following data processing procedure. First, we calculate the transient absorption signal $S(\tau, T, \omega_t, I) = -\log_{10}\frac{S_{\text{pumped}}(\tau,T,\omega_t,I)}{S_{\text{unpumped}}(\tau,T,\omega_t,I)}$. To Fourier transform with respect to τ, for each dataset $s(\tau) = S(\tau, T, \omega_t, I)$, we first reflect the signal to $-\tau$, without duplicating the $\tau = 0$ point and then perform the discrete Fourier transform, using Eq. S5.

The squaraine polymer linear absorption (Figure 4a) signal reveals two main peaks at 1.58 eV (A) and 1.87 eV originating from the absorption of the SQA and SQB sites. The J-type coupling leads to a further splitting of the peaks and the enhancement of the peak A at 1.58 eV in comparison to the separated monomer units.[1] The pump spectrum covers only the spectral region from the low-energy exciton peak at 1.58 eV (A) to the vibrational mode 1.73 eV (D), but not the high-energy exciton state at 1.87 eV.

The 1Q (around ω_0) and 2Q (around $2\omega_0$) regions of the raw data, used for extracting up to the $S_{(10)}$ spectra,

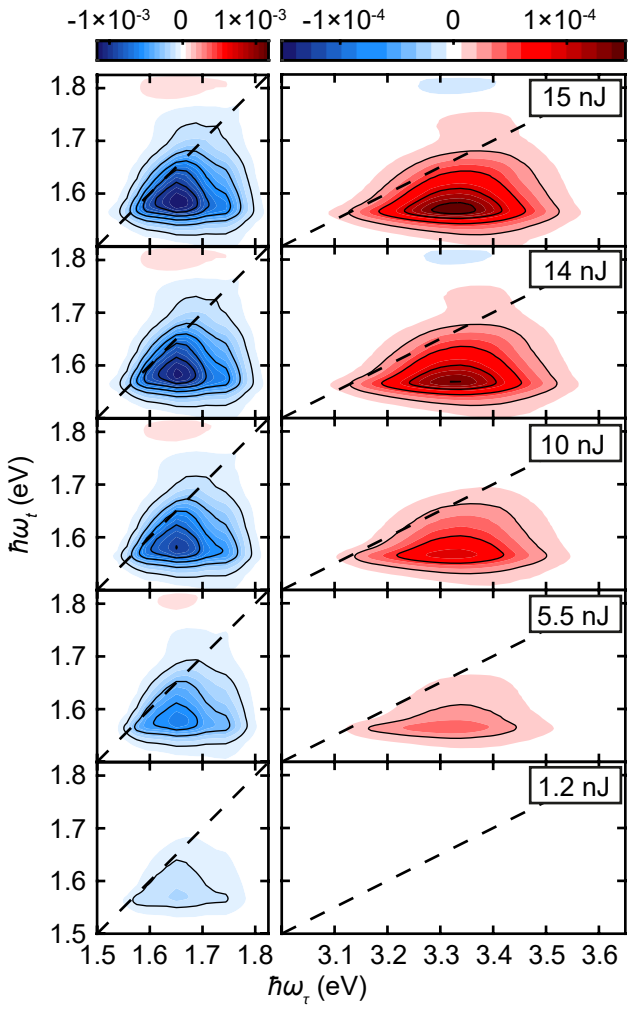

Figure S4: Raw 2D data at the 1Q and 2Q position taken at five different excitation intensities.

are shown in Figure S4. All 1Q and 2Q spectra display an intense signal slightly shifted below the diagonal, due to energy transfer taking place during the $T = 2$ ps population time.[2,3] The 1Q spectra are dominated by a negative feature, whereas the 2Q spectra exhibit a positive main feature. Additionally, a feature emerges at the blue edge of the ω_t axis (1.81 eV) in both nQ spectra, with its sign inverted relative to the corresponding main feature. With increasing excitation intensity, the absolute 2Q signal is enhanced compared to the 1Q signal.

Along ω_τ, the 1Q spectra display three distinct peaks, which correspond to the peaks in the absorption spectrum A, C, and D (Figure 4a). The signal maximum of all 1Q spectra lies at the C peak (1.65 eV) although the extracted order spectra exhibit a shift towards the redshifted peak A (Figure 4b). Moreover, the 2Q spectra exhibit an elongated shape without clearly separable peaks. The 2Q absolute signal maximum is blueshifted along ω_τ compared to twice the absolute signal maximum of the 1Q spectrum, agreeing with the predictions of Bubilaitis and Abramavičius for a model J-aggregate.[4]

S9 Comparison of lowest order with low-intensity reference measurement

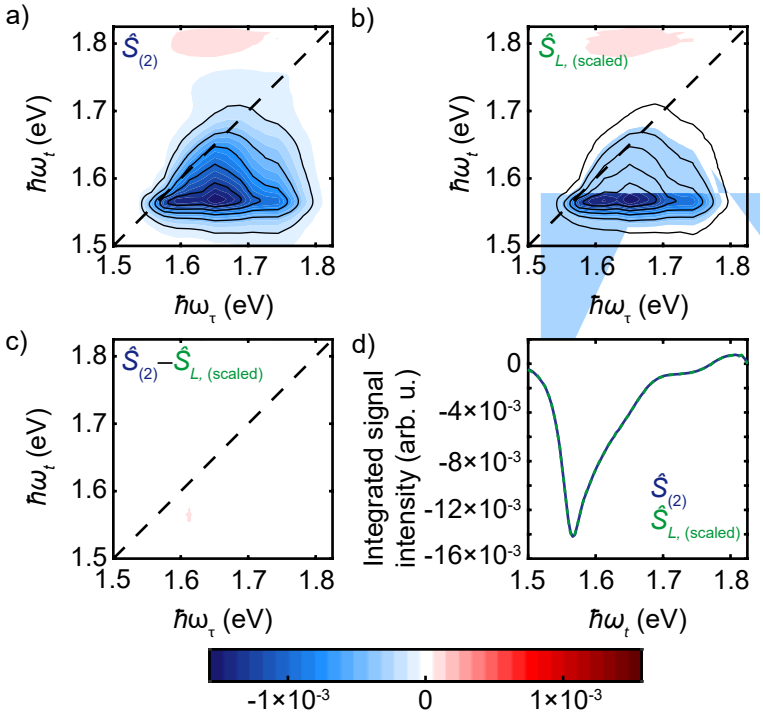

Figure S5: Lowest-order signal 1Q spectra. a) Extracted $\hat{S}_{(2)}$, b) Low-intensity reference measurement $S_{L,\mathrm{scaled}}$ scaled to I_0 (9 nJ). c) Scaled low-intensity measurement subtracted from the extracted $\hat{S}_{(2)}$. d) $\hat{S}_{(2)}$ and $S_{L,\mathrm{scaled}}$ integrated along ω_τ 1Q ($\omega_0[0.5, 1.5]$ for $\omega_0 = 1.59$ eV).

To verify the success of the extraction, we analyzed the integrated nQ signal of $S_{(2)}$ and $S_{(4)}$ (Figure 4b). For one further verification of the extraction of the lowest-order signal, we compare our extracted lowest order signal, $S_{(2)}$ (Figure S5a), with a low-intensity reference measurement, S_L (Figure S5b), detected at 0.16 nJ, where we assume

negligible higher-order contributions. To facilitate the direct comparison, we scale S_L to the reference power of the extraction $I_0 = 9$ nJ (Figure S5). The difference signal (Figure S5c) and the comparison of the integrated 1Q signals (Figure S5d) confirm the correct extraction of the pure third order.

S10 Visibility enhancement of cross peaks in higher-order signals

In the experimental data we see that there is a cross peak at the $(\omega_\tau, \omega_t) = (\omega_A, \omega_B)$ position that is visible in $S^{1Q}_{(4)}$ but does not appear in $S^{1Q}_{(2)}$. In this section we show that for a simple toy model the upper cross peak in the 1Q signal is frequently enhanced in the $S_{(4)}$ signal as compared with $S_{(2)}$. The high-order extraction thus gives visibility into this process even when it is not visible in the standard leading-order 2DES. The experimental data are for a polymer with on average 18 dimer subunits. For this theoretical discussion, we consider a dimer of two-level systems, which is the simplest possible model of a polymer. The fact that we see enhancement of the cross peak in $S_{(4)}$ as compared with $S_{(2)}$ for a wide range of parameters for such a simple model leads us to conclude that such effects can occur, and are perhaps even highly likely to occur, in polymer systems.

We describe our dimer with the Hamiltonian

$$H = \begin{pmatrix} \omega_g & 0 & 0 & 0 \\ 0 & \omega_a & J & 0 \\ 0 & J & \omega_b & 0 \\ 0 & 0 & 0 & \omega_f \end{pmatrix}, \tag{S32}$$

where $\hbar = 1$ and we take $\omega_g = 0$ and $\omega_f = \omega_a + \omega_b$, where there are four basis states $|g\rangle, |a\rangle, |b\rangle, |f\rangle$. The Hamiltonian can be diagonalized to find the eigenvalues $0, \omega_\alpha, \omega_\beta, (\omega_a + \omega_b)$, where

$$\begin{aligned} \omega_\alpha &= \frac{1}{2}\left(\omega_a + \omega_b - \sqrt{(\omega_a - \omega_b)^2 + 4J^2}\right), \\ \omega_\beta &= \frac{1}{2}\left(\omega_a + \omega_b + \sqrt{(\omega_a - \omega_b)^2 + 4J^2}\right), \end{aligned} \tag{S33}$$

corresponding to eigenstates

$$\begin{aligned} |\alpha\rangle &= \frac{1}{\sqrt{N}}\left[-\left(x + \sqrt{x^2+1}\right)|a\rangle + |b\rangle\right], \\ |\beta\rangle &= \frac{1}{\sqrt{N}}\left[|a\rangle + \left(x + \sqrt{x^2+1}\right)|b\rangle\right], \end{aligned} \tag{S34}$$

where $N = 2\left(x^2 + 1 + x\sqrt{x^2+1}\right)$ with $x = \frac{\omega_b - \omega_a}{2J}$. We define the splitting between the singly excited eigenvalues

$$\begin{aligned} \omega_{\beta\alpha} &= \omega_\beta - \omega_\alpha \\ &= \sqrt{(\omega_a - \omega_b)^2 + 4J^2} \end{aligned} \tag{S35}$$

and the average singly excited eigenvalue is

$$\omega_{\text{ave}} = \frac{\omega_\alpha + \omega_\beta}{2} = \frac{\omega_a + \omega_b}{2}. \tag{S36}$$

With this model, we explore the cross peak at $(\omega_\tau, \omega_t) = (\omega_A, \omega_B)$, so we fix $\omega_\alpha = \omega_A$ and $\omega_\beta = \omega_B$. With these two values set, there is a single free parameter in the Hamiltonian, J, which can vary from 0 to $\omega_{\beta\alpha}/2$. For $J = 0$, there cannot be cross peaks in a 2DES signal, since the two subsystems are uncoupled. As J increases, we expect that the cross peaks become more visible.

The dimer's dipole operator in the $|g\rangle, |a\rangle, |b\rangle, |f\rangle$ basis is

$$\mu = \begin{pmatrix} 0 & \mu_{ag} & \mu_{bg} & 0 \\ \mu_{ag} & 0 & 0 & \mu_{fa} \\ \mu_{bg} & 0 & 0 & \mu_{fb} \\ 0 & \mu_{fa} & \mu_{fb} & 0 \end{pmatrix}, \tag{S37}$$

where $\mu_{ij} = \langle i | \mu | j \rangle$, and we take $\mu_{fa} = \mu_{bg},\ \mu_{fb} = \mu_{ag}$. Transforming to the eigenbasis, we have

$$\begin{aligned} \mu_{\alpha g} &= \frac{1}{\sqrt{N}} \left[-\left(x + \sqrt{x^2+1} \right) \mu_{ag} + \mu_{bg} \right], \\ \mu_{\beta g} &= \frac{1}{\sqrt{N}} \left[\mu_{ag} + \left(x + \sqrt{x^2+1} \right) \mu_{bg} \right]. \end{aligned} \tag{S38}$$

Let us assume that we have a linear absorption spectrum with two well-resolved peaks. In such a case, ω_α, ω_β, $\mu_{\alpha g}$, and $\mu_{\beta g}$ are all known. Given these constraints, we can explore all possible dimer models that are consistent with this linear absorption spectrum, where there is a single free parameter, J, which can vary from 0 to $\omega_{\beta\alpha}/2$.

In the case of the experimental data, we know the splitting $\omega_{\beta\alpha}$ thanks to the cross peak visible in $S^{1Q}_{(4)}$, but we do not know the values of $\mu_{\alpha g}$ and $\mu_{\beta g}$, since the peaks overlap in the linear absorption spectrum. We will therefore consider three values of $\mu_r = \mu_{\alpha g}/\mu_{\beta g}$. We consider $\mu_r^2 = 0.5, 1, 2$. See the example linear absorption spectra for each of these three cases in Figure S6a where the spectra are normalized such that $\mu_{\alpha g}^2 + \mu_{\beta g}^2 = 1$. The ratio of the input dipole moments is

$$\frac{\mu_{bg}}{\mu_{ag}} = \frac{\mu_r + x + \sqrt{x^2+1}}{1 - \mu_r x - \mu_r \sqrt{x^2+1}}. \tag{S39}$$

Using the Ultrafast Spectroscopy Suite (UFSS)[5,6], we simulate the signals $S^{1Q}_{(2)}$ and $S^{1Q}_{(4)}$ due to impulsive pulses for population times $T\omega_{\beta\alpha} = 0.1, \pi/2, \pi$. We find the population time with the largest-magnitude cross peak, which we label T'. We then divide the cross-peak signal, $S_{(2n)}(\omega_A, T', \omega_B)$, by the absolute maximum signal $S^{\max}_{(2n)}(T') \equiv \max_{\omega_\tau, \omega_t} |S_{(2n)}(\omega_\tau, T', \omega_t)|$, to define the cross peak visibility as

$$\eta_{(2n)} = \frac{S_{(2n)}(\omega_A, T', \omega_B)}{S^{\max}_{(2n)}(T')}. \tag{S40}$$

We plot $\eta_{(2)}$ and $\eta_{(4)}$ in Figure S6b and the visibility enhancement $\eta_{(4)}/\eta_{(2)}$ in Figure S6c. The visibility enhancement

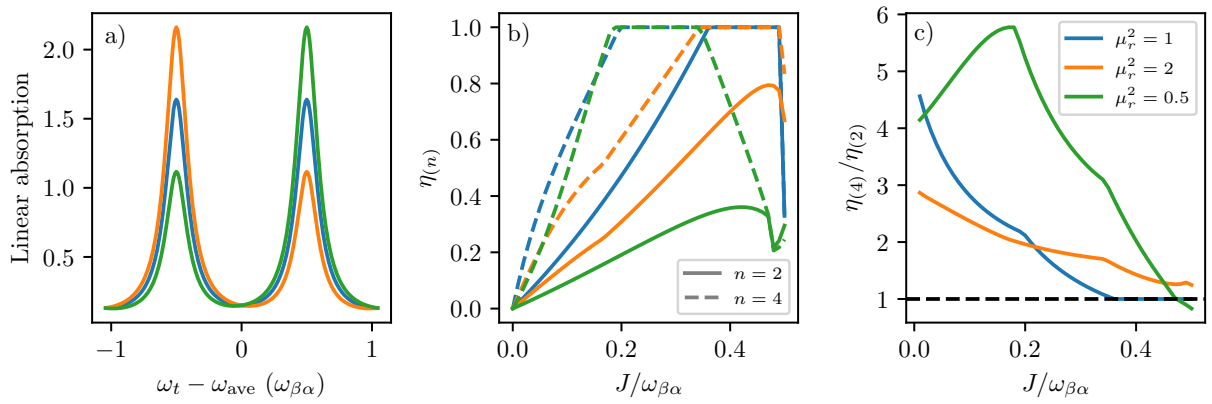

Figure S6: Dimer model. (a) Linear absorption for three choices of μ_r. (b) Visibility $\eta_{(n)}$ of $(\omega_\alpha, \omega_\beta)$ cross peak for $n = 2, 4$ and the three choices of μ_r shown in panel a. (c) Relative visibility enhancement showing that the cross peak is almost always more visible in $S_{(4)}$ than it is in $S_{(2)}$.

is nearly always greater than 1, except for J near its maximum value. In addition, the visibility enhancement is largest when visibility is small. This enhancement demonstrates the utility of measuring $S_{(4)}$, as it is a useful tool in uncovering cross peaks that might otherwise be hidden.

All of the calculations in this section are for a closed system and ignore the effects of a bath. The linear absorption spectra shown in Figure S6a are shown with a phenomenological linewidth of $\Gamma = 0.1\omega_{\beta\alpha}$, added after the simulations by multiplying the time-domain signal by $e^{-\Gamma t}$. However, the visibilities $\eta_{(2n)}$ are calculated by using a linewidth of $\Gamma = 0.01\omega_{\beta\alpha}$, This small linewidth ensures that the cross-peak position has negligible amplitude bleeding over from the diagonal peaks. When the linewidths are larger, the wings of the diagonal peaks can mask the cross peak. In this model, the upper-left cross peak in $S_{(2)}$ is always opposite in sign to the other three peaks for $J < 0.28$, and so the wings of the diagonal peaks can cancel with the cross peak, leaving little or no signal at that spectral location. We show two examples where the upper-left cross peak is not clearly visible in $S_{(2)}$ due to competition between a small but non-zero cross-peak signal and the wings of the diagonal peaks. Figures S7a and c show $S_{(2)}$ and $S_{(4)}$, respectively, for $J = 0.017\omega_{\beta\alpha}$ and the same linewidth used for Figure S6a. Figures S7b and d show $S_{(2)}$ and $S_{(4)}$, respectively, for $J = 0.1\omega_{\beta\alpha}$ and a Lorentzian linewidth of $\Gamma = 0.5$. Even though they come from a simple coupled-dimer model, panels b and d look qualitatively similar to the experimental results in Fig. 4b.

We further note that the cross peaks in a dimer model represent signals originating from transitions between both the ground state and the singly excited states, as well as signals originating from transitions between singly excited and doubly excited states. We have given all of these the same linewidth, but a more realistic model would have different linewidths, which would cause the cross peak to have more complicated shapes. However, we expect the qualitative argument to be the same: the $S_{(4)}$ signal should in general have higher visibility than $S_{(2)}$, and we expect there to be a considerable range of J in which the cross peak is hidden in $S_{(2)}$ but visible in $S_{(4)}$.

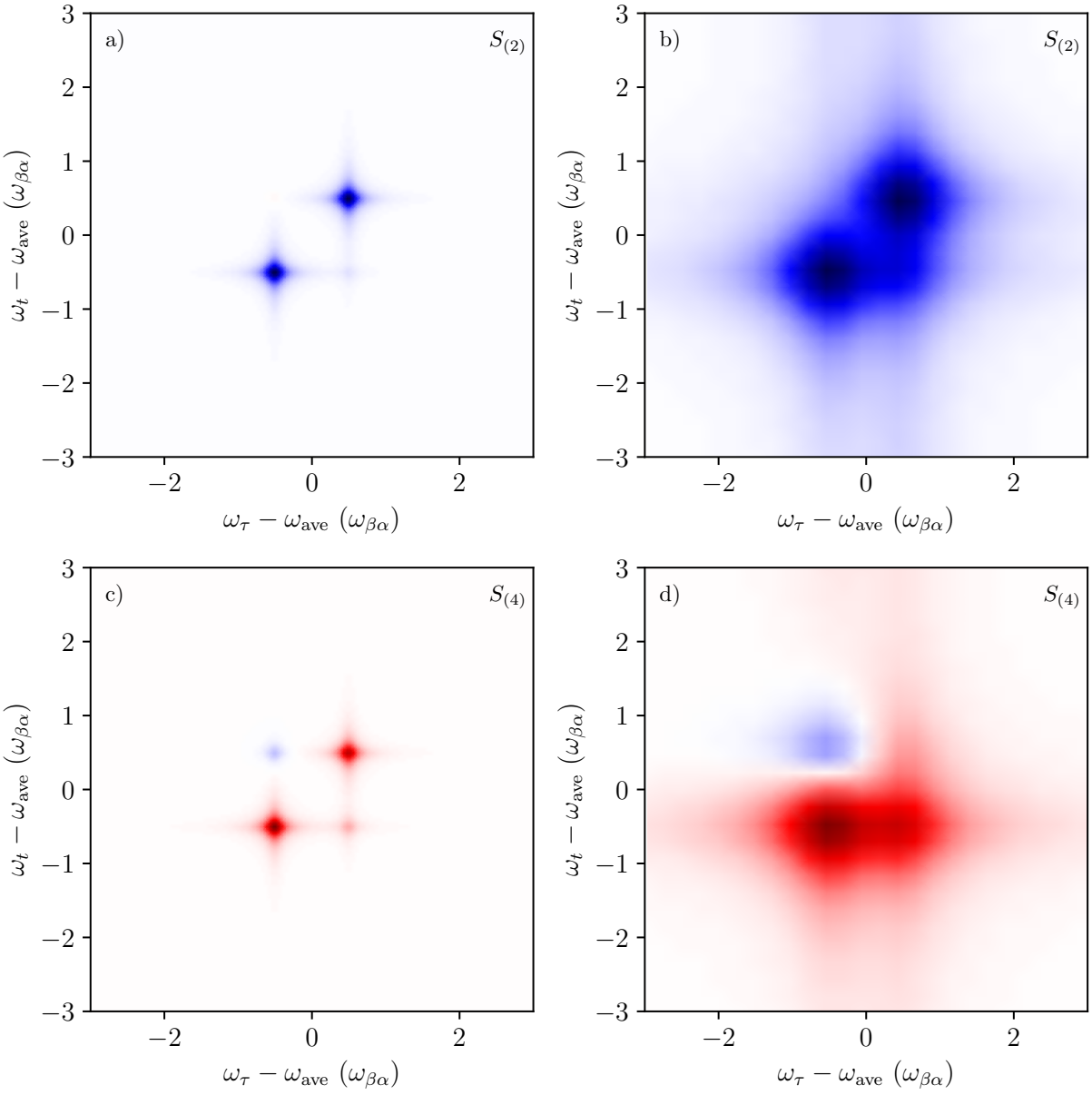

Figure S7: 1Q signals for the dimer model with $\mu_r = 1$, showing two different examples with no cross peak at position $(\omega_\tau, \omega_t) = (\omega_\alpha.\omega_\beta)$ visible at lowest order but clearly visible in $S_{(4)}$. (a) $S^{1Q}_{(2)}$ for $\Gamma = 0.1\omega_{\beta\alpha}$ and $J = 0.017\omega_{\beta\alpha}$. (b) $S^{1Q}_{(2)}$ for $\Gamma = 0.5\omega_{\beta\alpha}$ and $J = 0.1\omega_{\beta\alpha}$. (c) $S^{1Q}_{(4)}$ for $\Gamma = 0.1\omega_{\beta\alpha}$ and $J = 0.017\omega_{\beta\alpha}$. (d) $S^{1Q}_{(4)}$ for $\Gamma = 0.5\omega_{\beta\alpha}$ and $J = 0.1\omega_{\beta\alpha}$.

References

(1) Malý, P.; Lüttig, J.; Turkin, A.; Dostál, J.; Lambert, C.; Brixner, T. From wavelike to sub-diffusive motion: exciton dynamics and interaction in squaraine copolymers of varying length. *Chem. Sci.* **2020**, *11*, 456–466.

(2) Völker, S. F.; Schmiedel, A.; Holzapfel, M.; Renziehausen, K.; Engel, V.; Lambert, C. Singlet-Singlet Exciton Annihilation in an Exciton-Coupled Squaraine-Squaraine Copolymer: A Model toward Hetero-J-Aggregates. *J. Phys. Chem. C* **2014**, *118*, 17467–17482.

(3) Lambert, C.; Koch, F.; Völker, S. F.; Schmiedel, A.; Holzapfel, M.; Humeniuk, A.; Röhr, M. I. S.; Mitric, R.; Brixner, T. Energy transfer between squaraine polymer sections: From helix to zigzag and all the way back. *J. Am. Chem. Soc.* **2015**, *137*, 7851–7861.

(4) Bubilaitis, V.; Abramavicius, D. Signatures of exciton–exciton annihilation in 2DES spectra including up to six-wave mixing processes. *J. Chem. Phys.* **2024**, *161*, 104106.

(5) Rose, P. A.; Krich, J. J. Efficient numerical method for predicting nonlinear optical spectroscopies of open systems. *J. Chem. Phys.* **2021**, *154*, 034108.

(6) Rose, P. A.; Krich, J. J. Automatic Feynman diagram generation for nonlinear optical spectroscopies and application to fifth-order spectroscopy with pulse overlaps. *J. Chem. Phys.* **2021**, *154*, 034109.